

Machine-learning wall model of large-eddy simulation for low- and high-speed flows over rough surfaces

Rong Ma^{1*} and Adrián Lozano-Durán^{1,2}

¹Department of Aeronautics and Astronautics, Massachusetts Institute of Technology, Cambridge, MA 02139, USA

²Graduate Aerospace Laboratories, California Institute of Technology, Pasadena, CA 91125, USA

*rongma@mit.edu

Abstract

We present a wall model for large-eddy simulation (LES) that incorporates surface-roughness effects and is applicable across low- and high-speed flow regimes, for both transitional and fully rough conditions. The model, implemented using an artificial neural network, is trained on a database of direct numerical simulations (DNS) of compressible turbulent channel flows over rough walls. The dataset contains 372 cases spanning a wide range of irregular roughness topographies, including Gaussian and Weibull distributions, Mach numbers from 0 to 3.3, and friction Reynolds numbers between 180 and 2,000. We employ an information-theoretic, dimensionless learning method to identify the inputs with the highest predictive power for the dimensionless wall friction and wall heat flux. Predictions are also accompanied by a confidence score derived from a spectrally normalized neural Gaussian process, which quantifies uncertainty in regions that deviate from the training data distribution. The performance of the model is first evaluated *a-priori* on 110 turbulent channel flow cases, yielding prediction errors below 4%. The model is then assessed *a-posteriori* in wall-modeled large-eddy simulations (WMLES) across a diverse set of test cases. These include over 160 subsonic and supersonic turbulent channel flows with rough walls, a transonic high-pressure turbine (HPT) blade with Gaussian roughness, a high-speed compression ramp with sandpaper roughness, and three hypersonic blunt bodies with sand-grain roughness. Results show that the proposed wall model typically achieves *a-posteriori* predictive accuracy within 10% for wall shear stress and within 15% for wall heat flux, with high confidence in the channel flows and HPT blade cases. In the rough-wall compression ramp and hypersonic blunt bodies, the model captures the heating augmentation with errors ranging from 0% to 20%. In the cases with the highest errors, the reduced performance is correctly detected by a drop in the confidence score.

1 Introduction

Turbulent flows over rough surfaces in high-speed flow regimes present major challenges for both physical understanding and modeling. The compressibility effects on smooth walls, such as strong temperature gradients, aero-thermal coupling, and shock–boundary-layer interactions, have been extensively investigated and are known to fundamentally alter near-wall turbulence structures and transport mechanisms (Bradshaw, 1977; Papamoschou & Roshko, 1988; Zhang *et al.*, 2014; Nichols *et al.*, 2017; Yu *et al.*, 2019; Gaitonde & Adler, 2023). When surface roughness is present, these effects are further compounded, leading to enhanced drag, wall heating, and complex flow–surface interactions that are difficult to predict (Ekoto *et al.*, 2008; Tyson & Sandham, 2013; Modesti *et al.*, 2022; Jouybari *et al.*, 2023). In the context of LES, existing wall models, largely developed for smooth-wall or low-speed flows, usually fail to capture the coupled aero-thermal dynamics induced by roughness in high-speed flow regimes. Addressing these challenges requires improved physical insight and modeling strategies that can account for roughness effects in high-speed flows. In the present work, we develop a wall model for LES that accounts for subgrid-scale surface roughness and is applicable across a wide range of Mach numbers, from low- to high-speed regimes.

1.1 Physics of high-speed turbulence over rough surfaces

The flow physics of rough-wall turbulence have been extensively investigated in low-speed regimes (e.g., Orlandi & Leonardi, 2006; Schultz & Flack, 2007; Yuan & Piomelli, 2014; Ma *et al.*, 2021; Kadivar *et al.*, 2021) and, separately, for smooth-wall high-speed flows (Spina *et al.*, 1994; Guarini *et al.*, 2000; Pirozzoli *et al.*, 2008; Modesti & Pirozzoli, 2016; Zhang *et al.*, 2018; Cheng & Fu, 2024). In low-speed rough-wall turbulent boundary layers, surface roughness disrupts the near-wall cycle, leading to enhanced drag and a larger momentum deficit (Raupach *et al.*, 1991; Jiménez, 2004). The fully-rough regime is relatively well understood: form drag dominates and the wall friction becomes largely independent of Reynolds number. By contrast, the transitionally-rough regime remains challenging even at low speed. In this regime, viscous and form drag contribute simultaneously, rendering wall friction highly sensitive to Reynolds number and to the details of the surface topography. This sensitivity complicates the development of universal scaling laws and predictive drag models.

The challenges are further amplified at high speeds, where comparatively little attention has been devoted to rough-wall supersonic and hypersonic flows. The interplay among roughness, compressibility, and thermal effects introduces additional mechanisms that remain largely unresolved. In particular, roughness modifies near-wall temperature gradients and can weaken the Reynolds analogy between momentum and heat transfer (Kadivar *et al.*, 2021). Recent work by Kadivar & Garg (2025) further suggests that a universal rough-wall heat-transfer theory, even in low-speed flows, must account for multiple factors, including roughness topology, roughness thermal conductivity, roughness Reynolds number, and the Prandtl number.

To advance the understanding of compressible turbulent flows over rough surfaces, several experimental and DNS studies have been conducted. On the experimental front, the work of Latin & Bowersox (2000, 2002) examined the influence of various surface roughness configurations, including two uniformly distributed and three sand-grain roughness types, on the mean and turbulent properties of supersonic turbulent boundary layers. Their findings revealed that while kinematic turbulence quantities scaled with the local mean flow, thermodynamically dependent turbulence quantities exhibited a strong linear dependence on roughness height. Additionally, roughness was observed to extend the region where inner scaling holds for several turbulence intensity metrics. In a separate study, Ekoto *et al.* (2008) investigated the effects of large-scale periodic surface roughness on a supersonic turbulent boundary layer by comparing square and diamond roughness topologies against a smooth wall. They found that square roughness exhibited canonical rough-wall behavior, whereas the diamond pattern induced strong shock-expansion interactions that significantly distorted the flow and amplified turbulence production across the boundary layer.

From the computational side, several DNS of compressible flows over rough surfaces have been conducted over the past decade to investigate roughness effects. Muppidi & Mahesh (2012) used DNS to examine laminar-to-turbulent transition in a Mach 2.9 supersonic flat-plate boundary layer induced by distributed surface roughness. Similarly, Bernardini *et al.* (2012) performed DNS to analyze compressibility effects on boundary layer transition caused by an isolated three-dimensional cubic element in both low- and high-speed regimes. Both studies highlight the critical role of counter-rotating vortices in triggering transition, independent of Mach number. Tyson & Sandham (2013) conducted DNS of compressible turbulent channel flow over two-dimensional wavy rough surfaces at Mach numbers 0.3, 1.5, and 3. Their results indicate that at Mach 3, roughness peaks generate strong shock waves that significantly impact the mean flow across the entire channel. Modesti *et al.* (2022) carried out DNS of supersonic turbulent channel flows over distributed cubical roughness elements for Mach numbers ranging from 0.3 to 4. They found that while velocity statistics in the outer layer remain similar to those of smooth-wall flows, the thermal field is substantially modified by roughness throughout the channel core. Jouybari *et al.* (2023) performed DNS of supersonic turbulent channel flows over both two-dimensional and three-dimensional sinusoidal rough walls. Their findings demonstrate that flow behavior strongly depends on roughness topology: two-dimensional surfaces produce strong oblique shocks and elevated entropy generation, whereas three-dimensional surfaces generate only weaker shocklets.

The DNS studies of compressible flows discussed above have primarily focused on uniformly distributed regular roughness, with limited attention to more realistic, multiscale, and irregular roughness. In this work, we address this limitation by creating a DNS database of compressible turbulent channel flows over irregular Gaussian rough surfaces, spanning flow regimes from subsonic to supersonic, with bulk Mach numbers from 0.4 to 3.3 and bulk Reynolds numbers from 7,500 to 15,500. This database not only complements existing canonical datasets but also serves as a critical foundation for the training of our wall model.

1.2 Wall models for turbulence over rough surfaces

Modeling and prediction of roughness effects in rough-wall flows are essential tasks in engineering, as surface roughness can substantially amplify hydrodynamic drag and wall heat transfer, reducing the overall efficiency and durability of engineering systems (Bons, 2010; Chung *et al.*, 2021). In practical applications such as turbine blades in gas-turbine engines, and external surfaces of entry, landing, descent (EDL) vehicles, surface roughness arises from erosion, deposition, or thermal protection system (TPS) ablation (Bons, 2010; Hollis, 2014). Accurately capturing the impact of such roughness is crucial for predicting aerodynamic performance, heat loading, and material lifetime under realistic operating conditions. However, performing computational fluid dynamics (CFD) analysis with full-vehicle grids that explicitly resolve surface roughness is computationally prohibitive due to the extremely large number of grid cells required. While roughness-resolved simulations can provide valuable physical insight into the local flow structures and mechanisms, their applicability to high-Reynolds-number flows and realistic engineering configurations remains severely limited by the associated computational cost.

In the past decades, a range of models with differing levels of fidelity have been developed to capture wall-roughness effects, especially the drag induced by the roughness, spanning from empirical correlations derived from Moody charts to wall functions for Reynolds-averaged Navier–Stokes (RANS) simulations, as well as WMLES approaches (Flack & Schultz, 2010; Forooghi *et al.*, 2017; García-Mayoral *et al.*, 2024; Volino *et al.*, 2024; Zhou *et al.*, 2024). An extended overview of these modeling approaches for low-speed flows can be found in Ma & Lozano-Durán (2025). Many of these methods are developed based on the equivalent sand-grain roughness height k_s , which quantifies the hydrodynamic drag through a logarithmic relationship with the roughness function in the fully rough regime. However, k_s is not a purely geometrical parameter that can be directly inferred from the surface topology. Rather, it is a hydrodynamic parameter that characterizes the roughness effect on the flow and must be determined empirically through experiments or calibrated using high-fidelity simulations. This has limited the generalizability and applicability of the models.

Compared to low-speed flows, modeling for high-speed flows over rough surfaces poses additional challenges due to the complex coupling between aerodynamic and thermal processes (Bose & Park, 2018). In the context of EDL vehicles, roughness effects on aeroheating are typically modeled using RANS together with empirical correlations based on the roughness Reynolds number. For instance, in the Earth Entry System design, the Dahm roughness model has been applied in post-processing to estimate heating augmentation from surface roughness (Cheatwood *et al.*, 2024). However, this approach is inherently limited: correlations that rely solely on the roughness Reynolds number lack generality and may lose predictive accuracy across different roughness types, spatial distributions, and flow regimes. Moreover, RANS modeling for EDL flows faces additional challenges due to the complex aerodynamic and thermodynamic phenomena involved, including roughness-induced heat transfer and skin-friction enhancement in ablated TPS, separation behind blunt bodies, shock–boundary-layer interactions, high-enthalpy effects, and laminar-to-turbulent transition (Dirling, 1973; Finson & Clarke, 1980; Bowersox, 2007; Gaitonde & Adler, 2023). As noted by Hollis (2014), existing closure models often fail to capture these effects, particularly under conditions of strong compressibility and roughness-enhanced aero-thermal loads.

WMLES has demonstrated improved fidelity for high-speed flows (Kawai & Larsson, 2010; Yang *et al.*, 2018; Iyer & Malik, 2019; Mettu & Subbareddy, 2022; Chen *et al.*, 2022; Griffin *et al.*, 2023). By explicitly resolving the majority of length scales away from the wall while modeling the subgrid scales and the near-wall region, WMLES can improve predictions of wall shear stress, heat flux, and complex aero-thermal dynamics in supersonic and hypersonic regimes. In WMLES, the classical wall model for compressible flow consists of two coupled ordinary differential equations (ODEs) for velocity and temperature, solved with boundary conditions at the wall and the matching location—the interface between the wall-model layer and the LES outer layer (Cabot & Moin, 2000; Larsson *et al.*, 2016; Bose & Park, 2018). However, Fu *et al.* (2021) demonstrated that the iterative solution of this coupled boundary-value problem introduces greater nonlinearity than in the incompressible case and shows poor convergence in flows with large temperature gradients. The accuracy of the wall model also deteriorates under strong heat-transfer conditions, as observed by Griffin *et al.* (2023). Moreover, the mixing-length eddy viscosity model with two empirical constants (the von Kármán constant κ_v and the damping function constant A^+) commonly used for incompressible flow may not be appropriate for high-speed flows. Yang & Lv (2018) suggested that enhanced accuracy for high-speed flows over cold walls can be achieved through semi-local scaling in the damping function, while Iyer & Malik (2019) reported that the prediction of skin friction and wall heat flux in high-speed flows is sensitive to the values of κ_v and A^+ used in the eddy-viscosity model and damping function. Recently, Griffin *et al.* (2023) coupled a compressible velocity transformation that accurately represents both diabatic and adiabatic turbulent boundary layers (Griffin *et al.*, 2021), along with the temperature–velocity relationship (Zhang *et al.*, 2014), as the smooth-wall model for WMLES,

and obtained more accurate predictions of wall shear stress and heat transfer in cases with strong heat transfer. Nevertheless, existing wall models often neglect the critical role of surface roughness in shaping aero-thermal dynamics and still exhibit reduced accuracy when applied to flow over rough surfaces.

In our recent work (Ma & Lozano-Durán, 2025), we developed a rough-wall model for WMLES that directly leverages both geometrical roughness parameters and local flow information. This model, referred to as the *Building-Block-Flow Wall Model for Rough Walls* (BFWM-rough), builds upon our previous efforts on wall-modeling for low-speed and high-speed flows over smooth and rough walls (Lozano-Durán & Bae, 2023; Arranz *et al.*, 2024; Ma *et al.*, 2024; Ma & Lozano-Durán, 2025; Ling *et al.*, 2025). The approach is grounded in the idea that a limited set of canonical flow configurations, termed *building-block flows*, can encapsulate the essential physics required to accurately predict wall shear stress and heat flux in complex flow environments. The first version of BFWM-rough, introduced in Ma & Lozano-Durán (2025), was based on an artificial neural network trained on DNS of incompressible turbulent channel flows over rough walls. Validation results demonstrated superior accuracy compared to existing models in both canonical configurations and high-pressure turbine (HPT) blades, achieving prediction errors for wall shear stress within the range of 1% to 15% across both transitionally and fully rough regimes. In the present work, we re-design BFWM-rough to explicitly incorporate both compressibility and surface roughness effects. This new version is denoted as *BFWM-rough-v2*.

The manuscript is structured as follows: §2 introduces the roughness generation procedure and the DNS training database, comprising both incompressible and compressible flows. §3 provides an overview of the proposed wall model, the formulation of dimensionless inputs and outputs, details about the wall model training, and model uncertainty quantification. §4 presents *a-posteriori* results from WMLES applied to turbulent channel flows, HPT blade, a compression ramp, and three hypersonic blunt bodies with surface roughness. Concluding remarks are offered in §5.

2 DNS database

We conducted DNS of low- and high-speed turbulent channel flows over irregular rough surfaces. This DNS database forms the training set for the development of BFWM-rough-v2. The simulations were carried out using the minimal-span channel approach, following (Jiménez & Moin, 1991; Chung *et al.*, 2015; MacDonald *et al.*, 2017). As will be shown, these simulations can accurately reproduce near-wall flow dynamics, provided that the associated domain constraints are properly satisfied. Hereafter, the streamwise, wall-normal, and spanwise directions are denoted by x , y , and z , respectively. The channel half-height is denoted by δ . The details of surface roughness generation and DNS setups are described below.

2.1 Surface roughness generation

The roughness repository comprises a set of rough surface profiles designed to support the development of the DNS database used for training and validating the wall model. These surfaces are intended to reflect the variety of roughness types encountered in real-world engineering applications and are characterized by distinct probability density functions (PDFs) and power spectra (PS). Using a surface generator developed by Pérez-Ràfols & Almqvist (2019), irregular isotropic rough surfaces are synthesized based on prescribed PDFs and PS. Two primary statistical families are included: Gaussian and Weibull. The Gaussian distribution is selected due to its widespread occurrence in both natural and engineered systems (Williamson *et al.*, 1969; Whitehouse, 2023), while Weibull roughness is included to allow the repository to span a wider range of non-Gaussian and asymmetric roughness patterns, improving the generalization of the model across diverse surface conditions.

Following our previous work (Ma & Lozano-Durán, 2025), 19 Gaussian rough surfaces and 13 Weibull rough surfaces are used to create the rough-wall DNS database. A visualization of two roughness samples is shown in figure 1. The Gaussian roughness cases are labeled GS1 through GS19, while the Weibull roughness cases are labeled WB1 through WB13. Here, we summarize the range of key geometric roughness parameters represented in the roughness repository, including the root-mean-square roughness height (k_{rms}), mean roughness height (R_a), skewness (S_k), kurtosis (K_u), and effective slope (ES). The definitions of all roughness parameters are provided in Appendix A. The corresponding ranges, $1.1 < k_{rms}/R_a < 1.5$, $-0.7 < S_k < 2.2$, $2.2 < K_u < 12.0$, and $0.1 < ES < 0.7$, encompass a broad spectrum of surface characteristics representative of realistic roughness conditions encountered in engineering applications (Bons, 2010; Chung *et al.*, 2021).

We examined the correlation between pairwise roughness parameters, as shown in figure 2. The goal is to filter out parameters containing redundant information, enabling the identification of the subset of roughness parameters that most effectively inform the wall model. The candidate roughness parameters

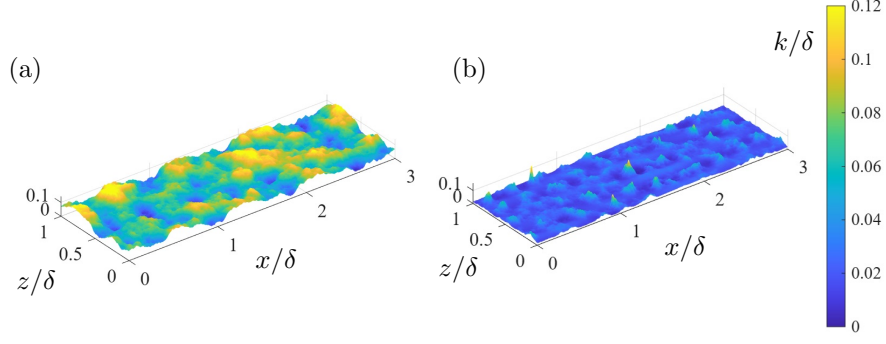


Figure 1: Roughness height (k) contour map of selected rough surface samples: (a) Gaussian roughness GS06; (b) Weibull roughness WB10. The roughness map is applied to turbulent channel walls, where δ is the channel half-height.

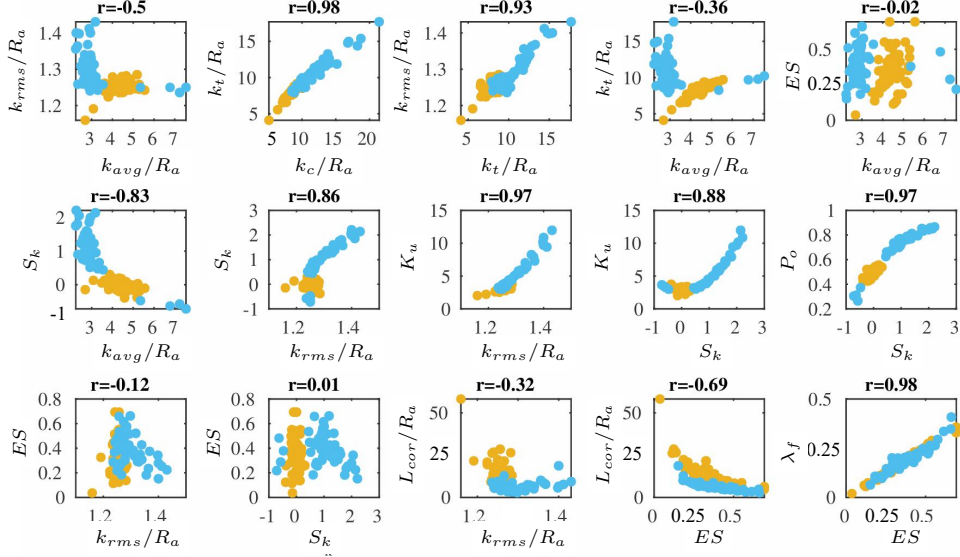


Figure 2: Scatter plot of pairs of roughness parameters and their correlation for Gaussian (orange) and Weibull (blue) rough surfaces.

considered include height-based measures such as mean roughness height k_{avg} , crest height k_c , mean peak-to-valley height k_t , root-mean-square height k_{rms} , and the first-order moment of height fluctuations R_a ; higher-order statistical parameters including skewness S_k and kurtosis K_u ; as well as spatial and geometric descriptors such as effective slope ES , surface porosity P_o , frontal solidity λ_f , and correlation length L_{cor} . The results show that k_{rms}/R_a is strongly correlated with k_t/R_a , k_c/R_a , S_k , K_u , and P_o , while only weakly correlated with k_{avg}/R_a , ES , and L_{cor} . In addition, ES shows a strong correlation with L_{cor} and λ_f , indicating that they contain redundant information. Therefore, the most representative parameters for input construction are k_{rms} , k_{avg} , R_a , and ES .

2.2 Incompressible channel flow database

The incompressible channel flow database was generated in our previous work (Ma & Lozano-Durán, 2025). The roughness tiles described in §2.1 are applied to the walls of open-channel flows. Although these simulations were performed in open channels, we use δ to denote the simulation height, for consistency with full-height channel notation. Turbulent open-channel flows over 32 rough surfaces were simulated using DNS at six distinct friction Reynolds numbers: $Re_\tau = u_\tau \delta / \nu = 180, 360, 540, 720, 900$, and 1,000, where u_τ is the friction velocity and ν is the kinematic viscosity. As a result, the database contains a total of 192 incompressible flow cases. The range of Re_τ values was determined based on the roughness Reynolds number $k_s^+ = k_s u_\tau / \nu$, which spans from 0 to 300 and represents conditions commonly observed in practical rough-wall flow scenarios, encompassing both transitionally rough and fully rough regimes. These simulations provide only the training data for the wall model that predicts the wall shear stress. To construct training data consistent with the compressible flow database, the flow variables such as

Case	M_b	Re_b	Re_τ	Re_τ^*	$-B_q$	Δx^+	Δy_{min}^+	Δy_{max}^+	Δz^+
M0.4-R7500	0.4	7500	416	403	0.004	3.12	0.06	3.74	2.60
M0.4-R10000	0.4	10000	550	532	0.004	4.13	0.08	4.95	3.44
M0.4-R15500	0.4	15500	818	795	0.004	4.09	0.12	7.36	3.41
M0.9-R7500	0.9	7500	432	373	0.016	3.24	0.06	3.89	2.70
M0.9-R10000	0.9	10000	570	493	0.015	4.28	0.09	5.13	3.56
M0.9-R10000	0.9	15500	862	744	0.014	4.31	0.13	7.76	3.59
M1.7-R7500	1.7	7500	490	309	0.06	3.68	0.07	4.14	3.06
M1.7-R10000	1.7	10000	660	400	0.05	4.95	0.10	5.94	4.13
M1.7-R15500	1.7	15500	970	600	0.05	4.85	0.15	8.73	4.04
M3.3-R7500	3.3	7500	671	194	0.19	5.03	0.10	6.04	4.19
M3.3-R10000	3.3	10000	869	251	0.16	4.35	0.13	7.82	3.62
M3.3-R15500	3.3	15500	1344	384	0.16	5.04	0.20	7.53	4.20

Table 1: Simulation parameters for the reference smooth-wall cases in the DNS database. Although not shown, for each reference case, 15 Gaussian-roughness simulations are performed, labeled as $GS\#-M\langle M_b \rangle-R\langle Re_b \rangle$. The friction Reynolds number is $Re_\tau = \rho_w u_\tau \delta / \mu_w$, with $u_\tau = \sqrt{\tau_w / \rho_w}$. The transformed friction Reynolds number is $Re_\tau^* = \rho_c u_\tau^* \delta / \mu_c$ (Coleman *et al.*, 1995), where $u_\tau^* = \sqrt{\tau_w / \rho_c}$ and the subscript c denotes mean quantities at the channel centerline. The wall heat-transfer rate is $B_q = q_w / (\rho_w c_p u_\tau T_w)$. Superscript + denotes viscous units based on u_τ and ν_w , where ν_w is the kinematic viscosity at the wall.

density, temperature, dynamic viscosity, and thermal conductivity, are set to constant values, and the bulk Mach number, defined as $M_b = U_b / \sqrt{\gamma R T_w}$, is set to 0.1, where U_b is the bulk velocity, γ is the ratio of specific heats, R is the specific gas constant, and T_w is the wall temperature. Here, “bulk” refers to averaging across the entire cross-section of the channel, as well as over time.

The flow solver integrates the incompressible Navier–Stokes equations and resolves the roughness geometry using an immersed boundary approach based on the volume-of-fluid method (Keating *et al.*, 2004; Yuan & Piomelli, 2014). The simulation domain has dimensions $(L_x, L_y, L_z) = (3\delta, \delta, \delta)$, following established guidelines for minimal-span channel simulations (Chung *et al.*, 2015; MacDonald *et al.*, 2017). Periodic boundary conditions are applied in the streamwise and spanwise directions, while no-slip and symmetry boundary conditions are enforced at the bottom and top boundaries, respectively. More details of the simulations and validation can be found in Ma & Lozano-Durán (2025).

2.3 Compressible channel flow database

The training dataset also includes DNS of compressible channel flows over irregular rough surfaces (Ma *et al.*, 2024). The rough-wall cases comprise 15 Gaussian rough surfaces created by specifying a Gaussian PDF and the power spectrum (PS) of isotropic self-affine fractals, following the method of Pérez-Ràfols & Almqvist (2019). The channel flows are driven by a uniform volumetric source term in the momentum and energy equations to achieve bulk Mach numbers $M_b = 0.4, 0.9, 1.7, 3.3$, and bulk Reynolds numbers $Re_b = \rho_b U_b \delta / \mu_w = 7,500, 10,000, 15,500$, where ρ_b is the bulk density and μ_w is the wall dynamic viscosity. In all simulations, the Prandtl number is $Pr = 0.72$, and the dynamic viscosity increases with temperature following a three-quarter power-law relationship, i.e., $\mu \propto T^{3/4}$.

The values $M_b = 0.4, 0.9, 1.7, 3.3$ are selected to cover subsonic and supersonic regimes relevant to practical conditions such as turbine blades (Nardini *et al.*, 2024) and high-speed vehicles (Hollis, 2014). In these cases, typical flow conditions yield k_s^+ values spanning nearly two orders of magnitude, from approximately $k_s^+ \sim 1$ to 200 (Bons, 2010; Hollis, 2014). Accordingly, $Re_b = 7,500, 10,000, 15,500$ are selected to achieve roughness Reynolds numbers in the range $0 < k_s^+ < 200$, where the flow spans transitionally rough and fully rough regimes. In total, the DNS database includes 180 rough-wall cases and 12 reference smooth-wall cases.

A summary of the reference simulation parameters is provided in Table 1. For the sake of brevity, only smooth-wall cases are reported. Each smooth-wall case is labeled using the convention $M\langle M_b \rangle-R\langle Re_b \rangle$; for example, M0.4-R7500 corresponds to a case with $M_b = 0.4$ and $Re_b = 7,500$. For each smooth-wall case, there are 15 rough-wall cases at similar M_b and Re_b , denoted by $GS\#-M\langle M_b \rangle-R\langle Re_b \rangle$, where “#” is the roughness index number. These are not shown in the table.

The DNS is conducted with the explicit, unstructured, finite-volume solver *charLES*, developed by Cascade Technology, which integrates the compressible Navier–Stokes equations. The solver has been previously used and validated in high-speed flows (Fu *et al.*, 2021). A sample visualization of the flow field

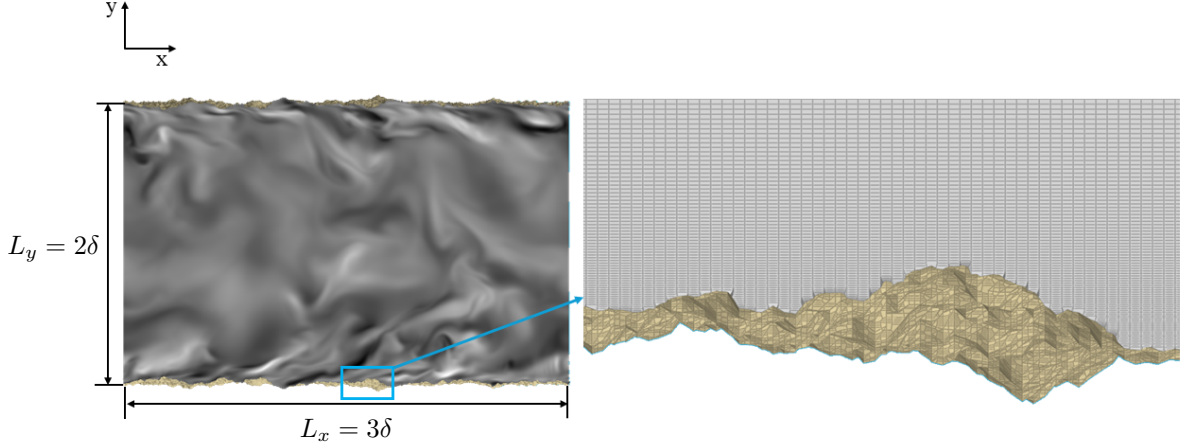


Figure 3: Instantaneous spanwise velocity normalized by the maximum spanwise velocity w/w_{\max} for DNS of a minimal-span channel flow over a rough wall. The contour legend is from -1 (black) to 1 (white). The case shown is GS1-M1.7-R10000. The zoom-in view shows the grid in the near-wall region. The wetted rough surfaces are colored in dark yellow.

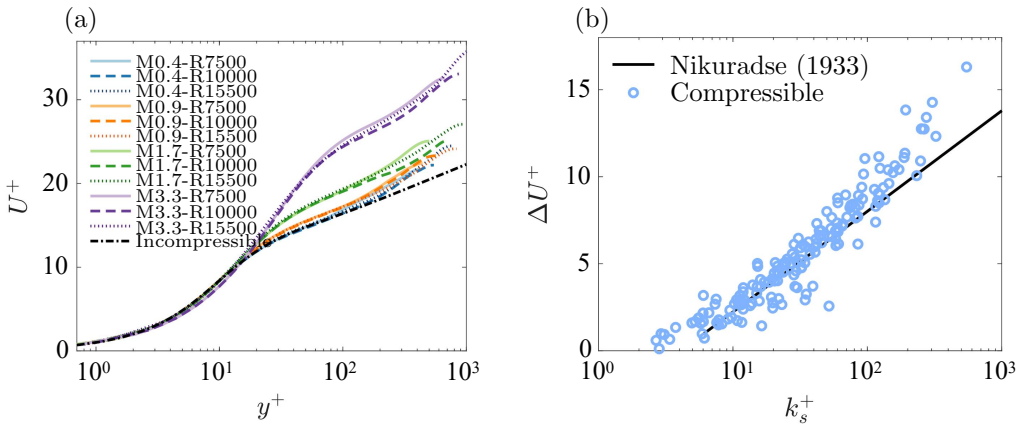


Figure 4: (a) Streamwise mean velocity profiles of smooth-wall reference cases, with a comparison to the incompressible channel flow DNS data from Lee & Moser (2015). (b) Roughness function ΔU^+ as a function of k_s^+ for current compressible channel flows with rough walls. The line denotes the Nikuradse's law for incompressible rough-wall turbulent flow (Nikuradse, 1933).

and near-wall mesh is presented in figure 3. The same minimal-span domain size as in the incompressible cases is employed, with $(L_x, L_y, L_z) = (3\delta, \delta, \delta)$. Uniform grid spacing is applied in the streamwise and spanwise directions, while a hyperbolic tangent stretching function is used to cluster points near the wall in the wall-normal direction. The grid resolution for smooth-wall cases is determined based on a grid convergence study. The rough-wall cases at the same M_b and Re_b are refined to achieve a grid resolution with $\Delta x^+ < 5$, $\Delta z^+ < 4.2$, and $\Delta y_{\min}^+ < 0.2$, which is comparable to the DNS of supersonic flows over roughness conducted by Modesti *et al.* (2022) and Jouybari *et al.* (2023). Figure 4 shows the streamwise mean velocity profiles of smooth reference cases and the roughness function against k_s^+ for each compressible rough case.

Validation of the minimal-span configuration against full-span simulations for both supersonic smooth- and rough-wall channel flows is presented in Appendix B. For the smooth-wall case, our DNS results show agreement with the reference DNS of Trettel & Larsson (2016), confirming both the accuracy of the flow solver and the validity of the minimal-span channel approach. Moreover, comparisons between minimal- and full-span rough-wall channel flows demonstrate agreement in the mean velocity profiles, with deviations within 3% for $y/\delta = 0.15$. Based on these results, the DNS mean data for $y/\delta < 0.15$ are deemed reliable and used to provide flow information for training the wall-model development.

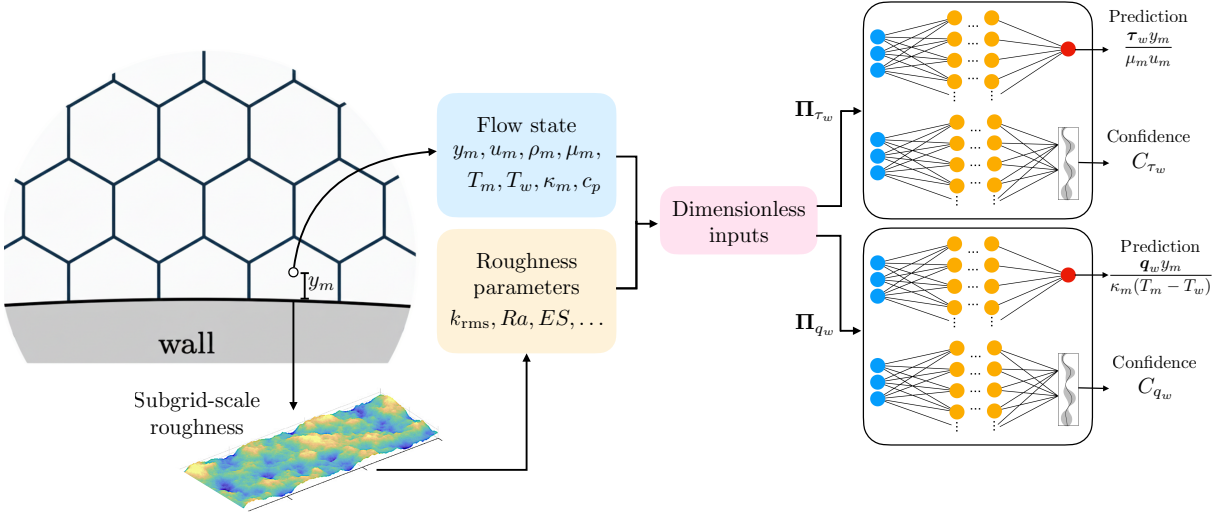


Figure 5: Overview of the proposed wall model (BFWM-rough-v2). The flow state at the wall and in the first off-wall control volume, together with statistical roughness parameters, are used to construct dimensionless inputs to the wall model. The model outputs the dimensionless wall-shear stress and wall heat flux, each accompanied by a confidence score. The wall-model mapping is represented with an FNN, while the confidence score in the prediction is quantified using an SNGP.

3 Formulation

3.1 Model overview

The wall model follows the building-block flow model principle introduced by Lozano-Durán & Bae (2023). The central assumption is that a set of simple, canonical flows can capture the essential physics needed to accurately predict wall shear stress and heat flux in more complex flow scenarios. Accordingly, it is postulated that a finite set of *building-block flows* (used as training data) encapsulates the relevant physics required to construct generalizable wall models. The building-block-flow concept has been applied to both subgrid-scale (SGS) models and wall models and the reader is referred to previous work for additional details (Lozano-Durán & Bae, 2020; Arranz *et al.*, 2024).

An overview of the proposed wall model is shown in figure 5. The approach is implemented using two feedforward neural networks (FNNs) that predict the dimensionless wall shear stress and wall heat flux, respectively:

$$\frac{\tau_w y_m}{\mu_m u_m} = \mathbf{ANN}_{\tau_w}(\Pi_{\tau_w}), \quad \frac{q_w y_m}{\kappa_m (T_m - T_w)} = \mathbf{ANN}_{q_w}(\Pi_{q_w}), \quad (1)$$

where Π_{τ_w} and Π_{q_w} are dimensionless inputs constructed from dimensional variables from both the wall and the first off-wall control volume located at height y_m (i.e., the matching location hereafter denoted by the subscript m). These variables include the density ρ_m , the magnitude of the wall-parallel velocity u_m , temperature T_m , wall temperature T_w , dynamic viscosity μ_m , thermal conductivity κ_m , and specific heat capacity c_p . The mean flow state, obtained through time and spatial averaging in the wall normal range $0.02 < y/\delta < 0.15$, is extracted from the DNS and used as input to the wall model. In addition, roughness parameters such as the root-mean-square roughness height k_{rms} , arithmetic mean roughness R_a , and effective slope ES , are also provided to the wall model. An information-theoretic dimensionless learning method (Yuan & Lozano-Durán, 2025) is employed to identify the most predictive inputs, as described in §3.3. The final input set used by the wall model is selected based on the minimum L_2 norm error achieved during the training process detailed in §3.4. To quantify model uncertainty and provide a confidence estimate, a Spectral-normalized Neural Gaussian Process (SNGP) is integrated into the model, as described in §3.5.

3.2 Modeling assumptions

We summarize the primary modeling assumptions underlying the BFWM-rough-v2 beyond those from WMLES.

- (i) *Building-block flow assumption:* A finite collection of canonical turbulent channel flows over rough surfaces, covering a range of Mach numbers, Reynolds numbers, and roughness geometries, contains

the essential physics required to construct a generalizable wall model for predicting both wall shear stress and wall heat flux.

- (ii) *Quasi-equilibrium assumption*: The near-wall region of rough-wall flows is assumed to be in a quasi-equilibrium state, i.e., the characteristic time scales of near-wall subgrid-scale motions affecting wall fluxes are much shorter than those of the grid-resolved large-scale motions.
- (iii) *Space/time locality assumption*: The local-in-space and local-in-time variables sampled at the first wall-normal control volume and at the wall (i.e., y_m , u_m , ρ_m , T_m , T_w , μ_m , κ_m and c_p) are assumed to contain sufficient information to predict the wall fluxes under assumption (ii).
- (iv) *Subgrid-scale roughness assumption*: Surface roughness is treated as a subgrid-scale feature whose primary effect on the resolved flow is represented via modified wall boundary conditions for momentum and energy (i.e., wall-shear stress and wall heat flux).
- (v) *Statistical roughness description assumption*: A finite set of statistical geometric parameters of the roughness (see Table 8) is assumed to be sufficient to characterize the influence of surface geometry on both wall momentum and heat transfer.
- (vi) *Velocity-shear and temperature-heat-flux alignment assumption*: The wall shear stress vector is assumed to be aligned with the local wall-parallel velocity at the first off-wall control volume in the WMLES grid. Similarly, the wall heat flux vector is assumed to be aligned with (and opposite to) the local temperature wall-normal gradient at the same location.
- (vii) *Dimensionless-form generalizability assumption*: The dimensionless form of the inputs and outputs, identified by maximizing predictability on the training set, remains valid across arbitrary flow configurations.
- (viii) *Mean-flow training data assumption*: Input-output samples constructed from mean velocity and temperature profiles, along with mean wall shear stress and wall heat flux, are assumed to provide sufficient information to train an accurate and generalizable wall model for compressible rough-wall flows.

3.3 Dimensionless learning for input variables

The model is formulated using dimensionless input and output variables to ensure dimensional homogeneity. The objective is to identify the minimal set of dimensionless input variables that retains strong predictive capability for the target output. The dimensional variables used to construct the dimensionless inputs include both flow and roughness information, denoted as $\mathbf{q} = [\mathbf{q}_{\text{flow}}; \mathbf{q}_{\text{roughness}}]$, where $\mathbf{q}_{\text{flow}} = [y_m, u_m, \rho_m, T_m, T_w, \mu_m, \kappa_m, c_p]^T$. The vector of roughness variables, $\mathbf{q}_{\text{roughness}}$, is left undefined at this stage. It may include parameters such as k_{avg} , k_{rms} , R_a , and ES (as discussed in §2.1). The optimal combination of these roughness parameters will be determined later. The goal is to minimize the number of geometric roughness features used by the model, as these quantities may not be readily available or may be difficult to quantify accurately in practical applications.

We used the dimensionless-learning method based on information developed by Yuan & Lozano-Durán (2025) to discover the most predictive dimensionless inputs for the wall model. We aim to find p dimensionless inputs that provide the highest predictive power of the dimensionless output Π_o . First, consider the generic dimensionless input $\mathbf{\Pi} = [\Pi_1, \dots, \Pi_p]$. The Buckingham- π theorem is applied to derive dimensionless groups $\mathbf{\Pi}$. Each dimensionless number Π_i takes the form $\Pi_i = \prod_{j=1}^n q_j^{a_{ij}} \equiv \mathbf{q}^{\mathbf{a}_i}$, where $\mathbf{a}_i = [a_{i1}, a_{i2}, \dots, a_{in}]^T$ is the exponent vector defining Π_i . These vectors are determined by solving the homogeneous linear system $\mathbf{D}\mathbf{a}_i = \mathbf{0}$, where \mathbf{D} is the dimension matrix containing the fundamental unit powers of each physical quantity q_j (i.e., $\mathbf{D} = [\mathbf{d}_1, \mathbf{d}_2, \dots, \mathbf{d}_n]$ with \mathbf{d}_j being the dimension vector of q_j). For example, if $q_1 = u$ (velocity) has dimensions [length]¹[mass]⁰[time]⁻¹[temperature]⁰, then $\mathbf{d}_1 = [1, 0, -1, 0]^T$. The general solution to $\mathbf{D}\mathbf{a}_i = \mathbf{0}$ can be written as a linear combination of basis vectors of the null space of \mathbf{D} : $\mathbf{a}_i = \sum_{j=1}^{n-k} c_{ij} \mathbf{w}_j = \mathbf{W}\mathbf{c}_i$, where $\mathbf{W} = [\mathbf{w}_1, \mathbf{w}_2, \dots, \mathbf{w}_{n-k}]$ spans the null space, $\mathbf{c}_i = [c_{i1}, c_{i2}, \dots, c_{i(n-k)}]^T$ are the coefficients and $k = 4$ is the number of fundamental units (i.e., length, mass, time, and temperature). Therefore, the resulting dimensionless input variables are given by $\mathbf{\Pi}(\mathbf{C}) \equiv \mathbf{q}^{\mathbf{WC}} = [\mathbf{q}^{\mathbf{WC}_1}, \mathbf{q}^{\mathbf{WC}_2}, \dots, \mathbf{q}^{\mathbf{WC}_p}]$, where the matrix $\mathbf{C} = [\mathbf{c}_1, \mathbf{c}_2, \dots, \mathbf{c}_p]$ can be freely chosen to define different candidate Π groups.

Although infinitely many dimensionless input combinations can be constructed, not all of them are optimal for predicting the dimensionless output. Our goal is to identify the input combination that offers the highest predictive power. Let the prediction error of a model \hat{f} , which estimates the output Π_o from input features $\mathbf{\Pi}$, be denoted by $\epsilon(\mathbf{\Pi}, \hat{f}) = \|\Pi_o - \hat{\Pi}_o\|_2$ where $\hat{\Pi}_o = \hat{f}(\mathbf{\Pi})$. The minimum achievable prediction error across all models \hat{f} is lower bounded by the information-theoretic irreducible error (Yuan

& Lozano-Durán, 2025):

$$\epsilon_{\min}(\boldsymbol{\Pi}) = \min_{\hat{f}} \epsilon(\boldsymbol{\Pi}, \hat{f}) \geq \frac{1}{\sqrt{2e\pi}} e^{h(\Pi_o) - I(\Pi_o; \boldsymbol{\Pi})}, \quad (2)$$

where $h(\Pi_o)$ is the differential entropy of the output and $I(\Pi_o; \boldsymbol{\Pi})$ denotes the mutual information between Π_o and the inputs $\boldsymbol{\Pi}$ (Cover, 1999). The differential entropy quantifies the expected uncertainty associated with the output variable Π_o , and is defined as

$$h(\Pi_o) = - \int f_{\Pi_o}(\pi_o) \ln f_{\Pi_o}(\pi_o) d\pi_o, \quad (3)$$

where f_{Π_o} denotes the probability density function of Π_o . The mutual information measures the amount of shared information between the output and the input variables, and is given by

$$I(\Pi_o; \boldsymbol{\Pi}) = \int f_{\boldsymbol{\Pi}, \Pi_o}(\boldsymbol{\pi}, \pi_o) \ln \left(\frac{f_{\boldsymbol{\Pi}, \Pi_o}(\boldsymbol{\pi}, \pi_o)}{f_{\boldsymbol{\Pi}}(\boldsymbol{\pi}) f_{\Pi_o}(\pi_o)} \right) d\boldsymbol{\pi} d\pi_o, \quad (4)$$

where $f_{\boldsymbol{\Pi}, \Pi_o}$ is the joint probability density function, and $f_{\boldsymbol{\Pi}}$, f_{Π_o} are the corresponding marginal densities of the input and output variables, respectively. Since $h(\Pi_o)$ is fixed for a given output, the best input candidate is the one that maximizes the mutual information:

$$\boldsymbol{\Pi}(\mathbf{C}) = \arg \max_{\boldsymbol{\Pi}} I(\Pi_o; \boldsymbol{\Pi}(\mathbf{C})) = \arg \max_{\mathbf{C}} I(\Pi_o; \boldsymbol{\Pi}(\mathbf{C})). \quad (5)$$

An advantage of using this method is that it provides an intrinsic predictability limit given the input and output variables, regardless of the modeling approach, allowing us to identify the most predictive inputs and outputs without the need to construct an explicit model.

This optimization problem can be efficiently solved using the Covariance Matrix Adaptation Evolution Strategy (CMA-ES) algorithm proposed by Hansen *et al.* (2003). The CMA-ES algorithm was used to find optimal combinations of inputs, with a population size of 50, coefficient bounds set to $[-2, 2]$, and a maximum of 50,000 iterations. The initial standard deviation for the search was set to 0.5.

To determine the minimum number of roughness parameters required in the wall-model inputs, we perform a dimensionless learning analysis by systematically varying both the combinations of roughness parameters and the number of dimensionless input variable. The results are summarized in Tables 2 and 3 for wall shear stress and wall heat flux predictions, respectively. These tables report $(1 - \tilde{\epsilon}_{LB})$, where $\tilde{\epsilon}_{LB}$ is the normalized irreducible error defined as (Yuan & Lozano-Durán, 2025)

$$\tilde{\epsilon}_{LB} = e^{-I(\Pi_o; \boldsymbol{\Pi})} \in [0, 1].$$

The quantity $(1 - \tilde{\epsilon}_{LB})$ measures the *degree of predictability* (akin to a generalized coefficient of determination) and represents the fraction of the target variable that can, in principle, be recovered from the available input information: a value of 0 indicates total unpredictability, whereas a value of 1 corresponds to perfect predictability.

Given a training database of size $O(10^4)$, the number of dimensionless inputs that can be reliably tested is limited to four, to ensure accurate estimation of the mutual information. Therefore, models are evaluated for $p = 1, 2, 3$, and 4. The results for $p = 1$ are omitted, as the analysis indicates that a single input yields poor scaling; at least two input parameters are required to capture meaningful relationships. An increase in p generally improves the degree of predictability across all parameter combinations, reflecting higher mutual information $I(\Pi_o; \boldsymbol{\Pi})$, as shown in Tables 2 and 3. We select the dimensionless input sets with $p = 4$ for both wall shear stress and wall heat flux. For wall shear stress, the chosen inputs consist of $[k_{avg}, R_a, ES]^T$ combined with \mathbf{q}_{flow} , while for wall heat flux, the selected model uses $[k_{rms}, ES]^T$ together with \mathbf{q}_{flow} ; these configurations are highlighted in green in Tables 2 and 3. Although including additional roughness descriptors can offer marginal improvements, the gains are minor and do not justify the increased model complexity.

The optimal dimensionless input combinations for predicting wall-shear stress are:

$$\boldsymbol{\Pi}_{\tau_w} = \arg \max_{\boldsymbol{\Pi}} I\left(\frac{\tau_w y_m}{\mu_m u_m}; \boldsymbol{\Pi}\right) = [\Pi_{\tau_w,1}, \Pi_{\tau_w,2}, \Pi_{\tau_w,3}, \Pi_{\tau_w,4}],$$

where

$$\begin{aligned} \Pi_{\tau_w,1} &= \frac{\left(\frac{T_m}{T_w}\right)^{0.2} Re_m^{0.7} Pr_m^{0.1} \left(\frac{y_m}{Ra}\right)^{0.1}}{M_m^{1.9} ES^{0.1}}, & \Pi_{\tau_w,2} &= \frac{Re_m^{0.4} M_m^{0.2} Pr_m \left(\frac{y_m}{k_{avg}}\right)^{0.1}}{\left(\frac{T_m}{T_w}\right) \left(\frac{y_m}{Ra}\right)^{0.5} ES^{0.4}}, \\ \Pi_{\tau_w,3} &= \frac{\left(\frac{T_m}{T_w}\right) Re_m^{1.2} Pr_m^{0.9} ES^{0.2}}{\left(\frac{y_m}{Ra}\right)^{0.1} M_m^{0.1}}, & \Pi_{\tau_w,4} &= \frac{\left(\frac{T_m}{T_w}\right)^{0.3} Re_m^{0.6} Pr_m^{0.5} \left(\frac{y_m}{k_{avg}}\right)^{0.2} ES^{0.5}}{\left(\frac{y_m}{Ra}\right)}. \end{aligned}$$

Flow quantity \mathbf{q}_{flow}	Roughness parameter $\mathbf{q}_{\text{roughness}}$	2 inputs		3 inputs		4 inputs	
		$1 - \tilde{\epsilon}_{LB}$	ϵ (%)	$1 - \tilde{\epsilon}_{LB}$	ϵ (%)	$1 - \tilde{\epsilon}_{LB}$	ϵ (%)
$y_m, u_m, \rho_m, T_m, T_w, \mu_m, \kappa_m, c_p$	k_{rms}, R_a	0.6732	15.78	0.6758	15.65	0.6790	14.92
	k_{avg}, R_a	0.6875	14.08	0.6882	11.87	0.6897	11.51
	k_{avg}, k_{rms}	0.6854	14.23	0.6878	12.95	0.7356	12.48
	k_{avg}, k_{rms}, R_a	0.6860	14.06	0.6882	11.66	0.6892	11.49
	k_{avg}, ES	0.6925	10.74	0.7058	10.09	0.7102	9.30
	k_{rms}, ES	0.7120	8.24	0.7275	5.37	0.7528	4.49
	R_a, ES	0.7135	7.82	0.7302	5.30	0.7511	4.91
	k_{rms}, k_{avg}, ES	0.7204	7.47	0.7352	5.25	0.7519	4.85
	k_{rms}, R_a, ES	0.7187	7.59	0.7253	5.63	0.7521	4.81
	k_{avg}, R_a, ES	0.7192	7.57	0.7350	5.25	0.7536	4.07
	$k_{avg}, k_{rms}, R_a, ES$	0.7199	7.49	0.7365	5.24	0.7539	4.04
	All parameters	0.7238	7.43	0.7386	5.21	0.7545	4.02

Table 2: Dimensionless-learning analysis for selecting inputs to the wall-shear-stress model. Table entries report the degree of predictability, $(1 - \tilde{\epsilon}_{LB})$, and the minimum L_2 -norm error, ϵ (%), achieved by an FNN for different combinations of roughness parameters included in the input. “All parameters” indicates that all candidate roughness parameters listed in Table 8 are included. The configuration highlighted in green, yielding $\epsilon = 4.07\%$, is selected as a compromise between predictability and the number of required roughness inputs.

Flow quantity \mathbf{q}_{flow}	Roughness parameter $\mathbf{q}_{\text{roughness}}$	2 inputs		3 inputs		4 inputs	
		$1 - \tilde{\epsilon}_{LB}$	ϵ (%)	$1 - \tilde{\epsilon}_{LB}$	ϵ (%)	$1 - \tilde{\epsilon}_{LB}$	ϵ (%)
$y_m, u_m, \rho_m, T_m, T_w, \mu_m, \kappa_m, c_p$	k_{rms}, R_a	0.7262	6.37	0.7323	5.56	0.7440	5.17
	k_{avg}, R_a	0.7281	6.14	0.7311	5.71	0.7471	5.57
	k_{avg}, k_{rms}	0.7272	6.17	0.7330	5.59	0.7433	5.40
	k_{avg}, k_{rms}, R_a	0.7292	6.08	0.7384	5.26	0.7525	5.12
	k_{avg}, ES	0.7123	7.06	0.7261	6.91	0.7482	6.79
	k_{rms}, ES	0.7344	5.44	0.7521	3.94	0.7753	2.89
	R_a, ES	0.7330	5.54	0.7542	3.91	0.7721	3.12
	k_{rms}, k_{avg}, ES	0.7360	5.32	0.7562	3.90	0.7749	2.83
	k_{rms}, R_a, ES	0.7323	5.54	0.7553	3.88	0.7802	2.85
	k_{avg}, R_a, ES	0.7351	5.47	0.7570	3.85	0.7783	3.02
	$k_{avg}, k_{rms}, R_a, ES$	0.7375	5.28	0.7610	3.79	0.7853	2.74
	All parameters	0.7384	5.26	0.7641	3.77	0.7884	2.62

Table 3: Dimensionless-learning analysis for selecting inputs to the wall-heat-flux model. Table entries report the degree of predictability, $(1 - \tilde{\epsilon}_{LB})$, and the minimum L_2 -norm error, ϵ (%), achieved by an FNN for different combinations of roughness parameters included in the input. “All parameters” indicates that all candidate roughness parameters listed in Table 8 are included. The configuration highlighted in green, yielding $\epsilon = 2.89\%$, is selected as a compromise between predictability and the number of required roughness inputs.

and for wall heat flux:

$$\Pi_{q_w} = \arg \max_{\Pi} I \left(\frac{q_w y_m}{\kappa_m (T_m - T_w)}; \Pi \right) = [\Pi_{q_w,1}, \Pi_{q_w,2}, \Pi_{q_w,3}, \Pi_{q_w,4}],$$

where

$$\begin{aligned} \Pi_{q_w,1} &= \frac{\left(\frac{T_m}{T_w}\right)^{0.2} Re_m^{0.7} M_m^{0.2} Pr_m^{0.3} ES^{0.3}}{\left(\frac{y_m}{k_{rms}}\right)}, & \Pi_{q_w,2} &= \left(\frac{T_m}{T_w}\right)^{0.9} Re_m^{1.8} M_m^{0.3} Pr_m^{1.0} \left(\frac{y_m}{k_{rms}}\right)^{0.1} ES^{0.2}, \\ \Pi_{q_w,3} &= \frac{Re_m^{0.7} \left(\frac{y_m}{k_{rms}}\right)^{0.1} ES^{0.1}}{\left(\frac{T_m}{T_w}\right) M_m^{0.2} Pr_m^{0.3}}, & \Pi_{q_w,4} &= \frac{\left(\frac{T_m}{T_w}\right)^{0.3} Re_m^{0.5} Pr_m}{\left(\frac{y_m}{k_{rms}}\right)^{0.5} ES^{0.7}}. \end{aligned}$$

Here, $M_m = u_m / \sqrt{\gamma R T_m}$, $Pr_m = c_p \mu_m / \kappa_m$, and $Re_m = \rho_m u_m y_m / \mu_m$ are the local Mach, Prandtl, and Reynolds numbers evaluated at the first grid point off the wall. Note that the temperature is assumed to be expressed on an absolute scale, where the minimum possible temperature corresponds to zero (e.g., Kelvin or Rankine). This ensures that ratios such as T_m/T_w can be interpreted as $(T_m - T_0)/(T_w - T_0)$ with $T_0 = 0\text{K}$. If the temperature is provided in a relative scale (e.g., degrees Celsius or Fahrenheit), it must first be converted to an absolute scale (e.g., by adding 273.15 for Celsius) to maintain consistency.

3.4 Wall model training

We train FNNs to construct wall models for τ_w and q_w using each input set listed in Tables 2 and 3. The network layers employ hyperbolic tangent sigmoid functions as activation functions, except for the output layer, which uses rectified linear units (ReLUs). Training is performed using gradient descent with momentum and an adaptive learning rate, following the backpropagation method (Yu & Liu, 2002). To mitigate overfitting, an L_2 regularization term with a factor of 0.9 is applied. To ensure robust model performance, 100 random splits of the data into training (70%), validation (15%), and testing (15%) sets are conducted for each input configuration. For every split, a grid search is used to identify the optimal network architecture, exploring configurations with 3 to 6 hidden layers and 5 to 20 neurons per layer. The minimum L_2 norm model error ϵ across different splits and network architectures is reported in Table 2 for wall shear stress and Table 3 for wall heat flux.

As expected, the model error decreases as the degree of predictability $1 - \tilde{\epsilon}_{LB}$ rises. For the wall shear stress, models incorporating both a roughness height parameter and ES exhibit significantly reduced errors, emphasizing the joint importance of height and slope statistics in predicting τ_w . For the wall heat flux, the inclusion of ES plays a less dominant role; combinations using k_{rms} (or R_a) and ES yield lower errors than those using k_{avg} and ES .

When increasing the number of inputs from 2 to 4, the model error typically decreases by approximately 3%. However, with only two or three inputs, some compressible cases still exhibit errors exceeding 40%, confirming that four inputs are necessary to ensure consistent scaling performance. As a result, the model for wall shear stress achieves an error of $\epsilon = 4.07\%$, and the model for wall heat flux attains an error of $\epsilon = 2.89\%$.

The PDFs of the *a-priori* error in figure 6 show the distribution of prediction errors for the training, validation, and testing datasets, corresponding to the dataset split used during the training of the optimal model. The resemblance of the error distributions across these datasets indicates that the model for both τ_w and q_w performs consistently, regardless of whether it is evaluated on seen (training) or unseen (validation and testing) data. This similarity confirms that the model is not overfitting to the training data and maintains predictive accuracy on new samples.

3.5 Model confidence score

The model includes an additional module that outputs a *confidence score* alongside each prediction, providing separate scores for the wall shear stress and wall heat flux estimates. The central idea is to quantify how far a previously ‘unseen’ input lies from the training data distribution: inputs that are close to the training data are expected to yield high confidence, whereas inputs that are far from it are flagged as potentially unreliable (low confidence). We implement this distance-to-training principle using the Spectral-normalized Neural Gaussian Process (SNGP) approach, which enhances the distance-awareness and calibration of deep neural networks. We adapt SNGP by introducing a Bayesian linear regression output layer, and then map the resulting predictive uncertainty to a scalar confidence score via an empirical cumulative distribution function (ECDF).

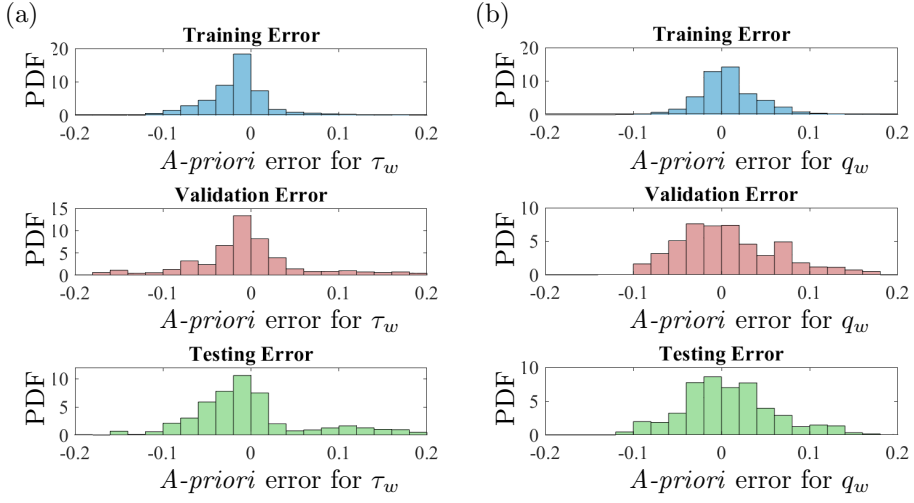


Figure 6: PDFs of *a-priori* relative error of BFWM-rough-v2 for the training, validation, and testing datasets: (a) wall shear stress and (b) wall heat flux. The relative error is computed by $(\tau_{w,\text{predict}} - \tau_{w,\text{true}})/\tau_{w,\text{true}}$ for τ_w and $(q_{w,\text{predict}} - q_{w,\text{true}})/q_{w,\text{true}}$ for q_w .

3.5.1 SNGP

A Gaussian process (GP) with an appropriate kernel is a well-known method that can achieve distance awareness (Rasmussen & Williams, 2006). This was used to obtain confidence in our previous version of the model (Ma & Lozano-Durán, 2025). However, it often generalizes poorly to high-dimensional data, as standard kernels may fail to capture the intrinsic structure, leading to degraded performance due to the curse of dimensionality. On the other hand, a standard neural network is not distance-aware, since the hidden mapping is not constrained to preserve geometric relationships from the input space.

To address the limitations above, we use the SNGP introduced by Liu *et al.* (2023). The approach produces uncertainty estimates using a single deterministic model representation. It is built on the principle of distance awareness, which asserts that the predictions of the model should account for the distance between new test inputs and the training data. This property is essential for achieving high-quality uncertainty quantification, as several prior studies have highlighted the close connection between a neural network's uncertainty performance and its ability to discern distances in the input space (Kristiadi *et al.*, 2020; Van Amersfoor *et al.*, 2021).

The details of the implementation are discussed in Appendix C. Here, we provide a brief overview of the method. For an input $\mathbf{\Pi}$ with feature representation $\phi = \phi(\mathbf{h}(\mathbf{\Pi}))$, where \mathbf{h} denotes a spectrally-normalized deep neural network feature extractor, the SNGP output layer models the scalar response Π_o using a Bayesian linear regression in feature space. The posterior of the regression weights β yields the predictive probability distribution of Π_o conditioned on $\mathbf{\Pi}$

$$f_{\Pi_o|\mathbf{\Pi}} = \mathcal{N}\left(\mu_\beta^\top \phi, \phi^\top \Sigma_\beta \phi + \sigma_n^2\right), \quad (6)$$

where \mathcal{N} is the normal distribution, μ_β and Σ_β are the posterior mean and covariance of β , and σ_n^2 is the observation-noise variance. The predictive variance decomposes into $\phi^\top \Sigma_\beta \phi + \sigma_n^2$. The first term, $\sigma_e^2 = \phi^\top \Sigma_\beta \phi$, captures epistemic uncertainty, which typically increases for inputs whose feature representations are far from those observed in training, reflecting lack of model knowledge. The second term, σ_n^2 , captures aleatoric uncertainty due to irreducible observation noise. In this work, σ_e^2 is used to construct a predictive confidence score.

The SNGP model is trained using the same DNS database employed for the wall model, with identical input features and output targets. The input features are normalized to the range $[0, 1]$ based on their componentwise extrema in the training dataset, while the output targets are standardized to have zero mean and unit variance. Training is performed using the Adam optimizer with a learning rate of 10^{-3} , a batch size of 128, and a total of 100 training epochs. A validation split of 15% of the training data is used to monitor convergence and prevent overfitting.

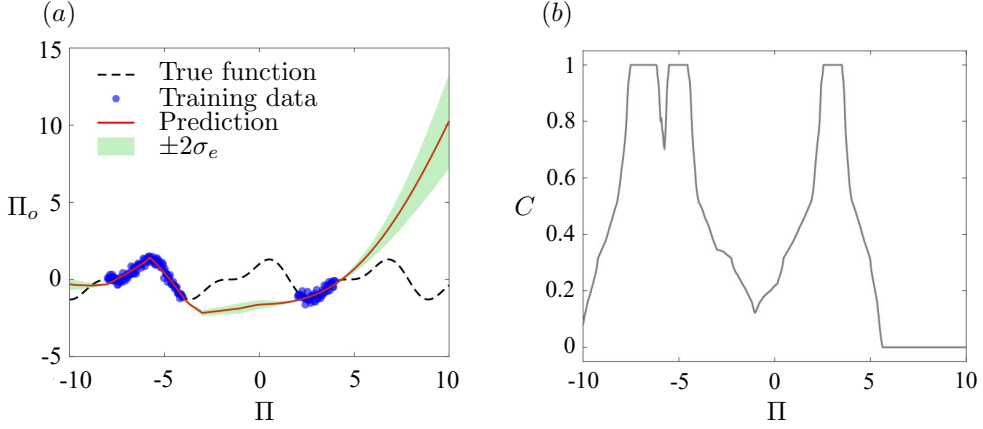


Figure 7: Demonstration of confidence score on a 1-D problem: (a) prediction and uncertainty results and (b) confidence score.

3.5.2 Confidence score

To calibrate the confidence, we construct a reference distribution of epistemic uncertainty across the normalized input space. This procedure enables us to transform a raw value of σ_e from any test point into a percentile-based confidence score, reflecting how typical or atypical the uncertainty of the model is relative to a broad set of reference cases. Specifically, we generate a large pool of reference inputs ($N_{\text{ref}} = 20,000$ samples) in the normalized input domain. This contains training points and random draws. For each reference input, the epistemic uncertainty σ_{ref} is computed using the SNGP model. The collection of these values is then sorted and stored as a reference distribution.

During evaluation, for a given testing point Π , a test-point uncertainty $\sigma_e(\Pi)$ can be mapped to its corresponding percentile in this distribution, yielding a value for the confidence score. The ECDF is defined as

$$F(\sigma_e) = \frac{1}{N_{\text{ref}}} \sum_{i=1}^{N_{\text{ref}}} \mathbf{1}\{\sigma_{\text{ref},i} \leq \sigma_e\}, \quad (7)$$

where $\mathbf{1}\{\cdot\}$ is the indicator function. The confidence score is then mapped as

$$C(\Pi) = 1 - F(\sigma_e(\Pi)). \quad (8)$$

Thus, low epistemic uncertainty corresponds to high confidence, while inputs far from the training distribution yield higher epistemic variance and lower confidence.

3.5.3 Demonstration of confidence score on a 1-D problem

We illustrate the performance of the confidence score in a simple one-dimensional problem. The ground-truth function is defined as $\Pi_o = \cos(\Pi) + 0.5 \sin(2\Pi)$, $\Pi \in [-10, 10]$. Training data are intentionally restricted to two narrow subregions, $[-8, -4]$ and $[2, 4]$, leaving large intervals of the input space unobserved. To mimic realistic measurement noise, Gaussian perturbations are added to the training labels.

Figure 7(a) shows the results. In the observed training regions, the model accurately recovers the functional form, with low uncertainty bands. In contrast, in unobserved intervals such as $[-10, -8]$, $[-4, 2]$, and $[4, 10]$, the epistemic error (σ_e^2) grows systematically. Figure 7(b) shows the confidence score as a function of the input location Π . In regions covered by training data, the model maintains high confidence ($C \approx 1$), consistent with its accurate predictions and low predictive variance. Conversely, in regions far from the training intervals, confidence decreases sharply, reflecting the reduced reliability of the model.

4 Validation

The performance of BFWM-rough-v2 is assessed *a-posteriori* in WMLES across a broad range of flow configurations. All validation cases are unseen during model training. These include a total of 162 incompressible and compressible turbulent channel flows, a high-pressure turbine (HPT) blade with Gaussian roughness, a compression ramp with sandpaper roughness, and three hypersonic blunt bodies with sand-grain roughness.

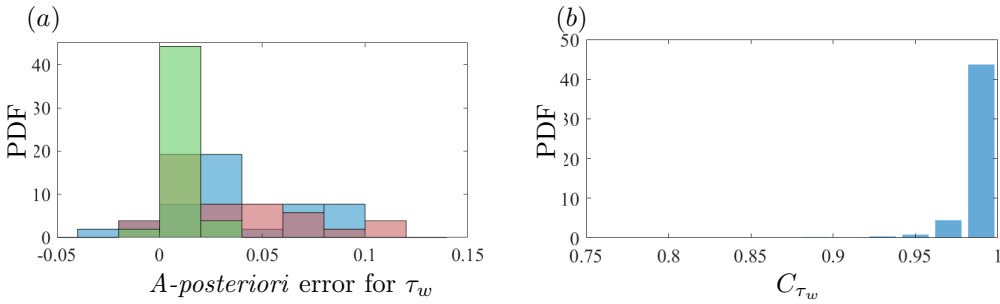


Figure 8: *A-posteriori* evaluation of BFWM-rough-v2 in WMLES of incompressible turbulent channels. PDFs of (a) relative error in wall shear stress and (b) space-time averaged confidence score. Results are shown at three different grid resolutions: $\Delta/\delta = 1/20$ (blue), $1/10$ (red), and $1/5$ (green).

It is also useful to decompose the wall model errors into two primary sources (Lozano-Durán & Bae, 2023): (i) *external errors*, which arise from inaccuracies in the outer LES input data at the wall-model interface, and (ii) *internal errors*, which are associated with the physical assumptions inherent to the wall model itself. External errors are typically dominated by deficiencies in the SGS model, while internal errors persist even when exact inputs are provided, particularly if model assumptions, e.g., quasi-equilibrium, locality, or training on mean data (see §3.2) are violated. The sum of these two contributions constitutes the *total error*. The *internal errors* of BFWM-rough-v2 were assessed earlier in Figure 6 using DNS as input data. Here, we focus on the *total error* in actual WMLES to assess the overall predictive performance of the model.

The BFWM-rough-v2 was implemented into the high-fidelity solver charLES, developed by Cascade Technologies, Inc (Bres *et al.*, 2018; Fu *et al.*, 2021). For all the validation cases, the Vreman SGS model (Vreman, 2004) is employed in the WMLES. The computational mesh is generated by performing a Voronoi tessellation of a set of seed points.

For comparison purposes, we employ an algebraic equilibrium wall model with prescribed k_s based on the rough-wall logarithmic law. The wall heat flux is computed using an algebraic approximation derived from the temperature law of the wall. We denote these two models for wall shear stress and wall heat flux collectively as “EQWM- k_s ”. The detailed formulation of EQWM- k_s is provided in Appendix D. Similar models have previously been applied to low-speed flows, although their applicability to high-speed regimes remains limited (Li *et al.*, 2022; Kadivar & Garg, 2025). It is important to note, however, that EQWM- k_s requires specification of k_s , a flow-dependent parameter. In the cases below, k_s is obtained directly from DNS data or from a simple correlation-based model calibrated for the case under consideration. As such, EQWM- k_s is not a truly predictive model, but rather a reference for assessing the performance of a wall model under the equilibrium rough-wall logarithmic-law assumption.

4.1 Turbulent channel flow

4.1.1 Incompressible flow

We conduct WMLES with BFWM-rough-v2 for incompressible turbulent channel flows over rough surfaces. The computational domain dimensions are set to $L_x = \pi\delta$, $L_y = 2\delta$, and $L_z = 0.5\pi\delta$. The test cases are drawn from the testing dataset introduced in §3.4, and include 12 Gaussian and 9 Weibull rough surfaces spanning $Re_\tau = 180$ to 1000 and $k_s^+ = 5$ to 230. The model performance is evaluated at three different grid resolutions: $\Delta/\delta = 1/20$, $1/10$, and $1/5$. In total, 78 unseen incompressible turbulent channel flow cases are tested.

Figure 8 presents the PDFs of the *a posteriori* error in the model predictions and the space-time averaged confidence score. Results for the three different grid resolutions, $\Delta/\delta = 1/20$, $1/10$, and $1/5$, are shown in blue, red, and green, respectively. The error distributions remain within 15% across all grid spacings, with the majority of cases exhibiting errors below 5%. Regarding model confidence, most cases cluster near $C = 1$, where the PDF exhibits a sharp peak, indicating high confidence in the predictions for the majority of testing cases. Only a few cases fall within the lower confidence range of $0.75 < C < 0.9$.

The WMLES results using EQWM- k_s for the same testing cases are shown in figure 9, exhibiting errors within 5%, which are smaller than those obtained with BFWM-rough-v2. This outcome is expected, as the true k_s value extracted from DNS is prescribed in EQWM- k_s to enforce the correct momentum deficit in the incompressible flow.

Figure 10 compares the mean velocity profiles from WMLES with DNS results for four selected cases spanning different roughness types and Re_τ . Overall, the WMLES results show reasonable agreement

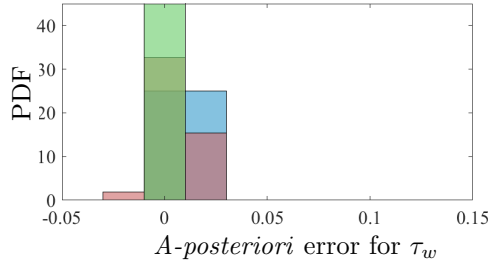


Figure 9: *A-posteriori* evaluation of EQWM- k_s in WMLES of incompressible turbulent channels. PDFs of *a-posteriori* relative error in wall shear stress. Results are shown at three different grid resolutions: $\Delta/\delta = 1/20$ (blue), 1/10 (red), and 1/5 (green).

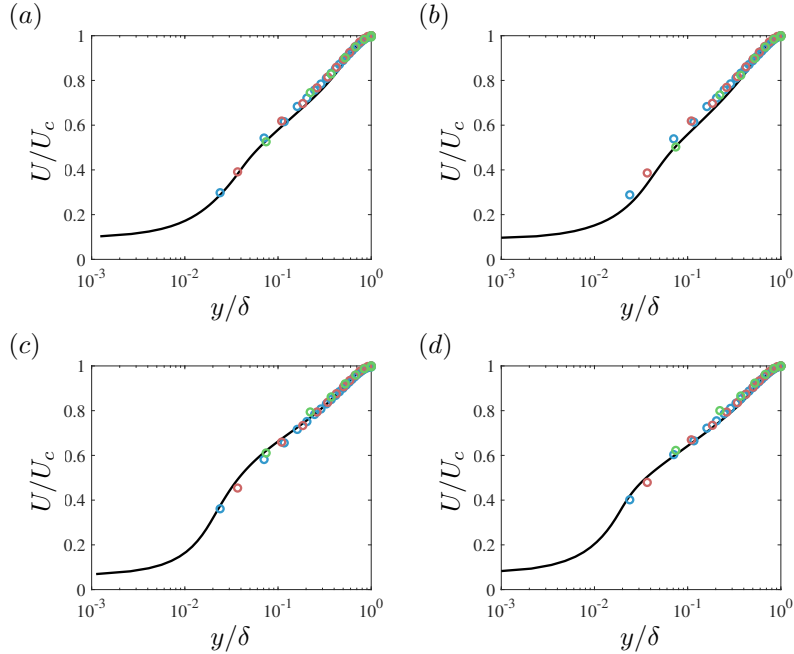


Figure 10: *A-posteriori* evaluation of BFWM-rough-v2 in WMLES of incompressible turbulent channels. Mean velocity profiles for DNS (line) and WMLES (symbols) for (a) GS3 at $Re_\tau=720$; (b) GS11 at $Re_\tau=900$; (c) WB8 at $Re_\tau=540$; (d) WB11 at $Re_\tau=1000$. Results are shown at three different grid resolutions: $\Delta/\delta = 1/20$ (blue), 1/10 (red), and 1/5 (green).

with DNS across all grid resolutions for the selected test cases.

4.1.2 Compressible flow

The BFWM-rough-v2 model is next validated in the WMLES of compressible turbulent channel flow over rough walls. Simulations are conducted in a domain of size $L_x = \pi\delta$, $L_y = 2\delta$, and $L_z = 0.5\pi\delta$. The test dataset, described in §3.4, is evaluated at three grid resolutions: $\Delta/\delta = 1/20$, 1/10, and 1/5. These tests encompass 12 Gaussian rough surfaces, spanning bulk Mach numbers from $M_b = 0.4$ to 3.3, bulk Reynolds numbers from $Re_b = 7,500$ to 155,000, and roughness Reynolds numbers from $k_s^+ = 5$ to 170. In total, 84 cases are examined.

Figure 11 shows the PDFs of the relative error in wall shear stress and heat flux. The model performance is assessed at the three grid resolutions mentioned above, represented by blue, red, and green curves, respectively. The mean relative errors for τ_w and q_w are 3.82% and 7.85%, respectively. Errors in τ_w remain within 15%, while larger errors of up to 30% are observed for q_w in some testing cases. Despite this, the majority of test cases still exhibit high confidence scores ($0.9 \leq C \leq 1$) for both wall shear stress and wall heat flux predictions. The confidence score distribution for τ_w is sharply peaked around 1, indicating strong model certainty. While the confidence score for q_w also peaks at 1, it displays a broader distribution with greater weight in the lower-confidence range.

For comparison, WMLES using EQWM- k_s are also performed, and the results are presented in figure 12. The errors in both wall shear stress and wall heat flux are larger than those obtained with

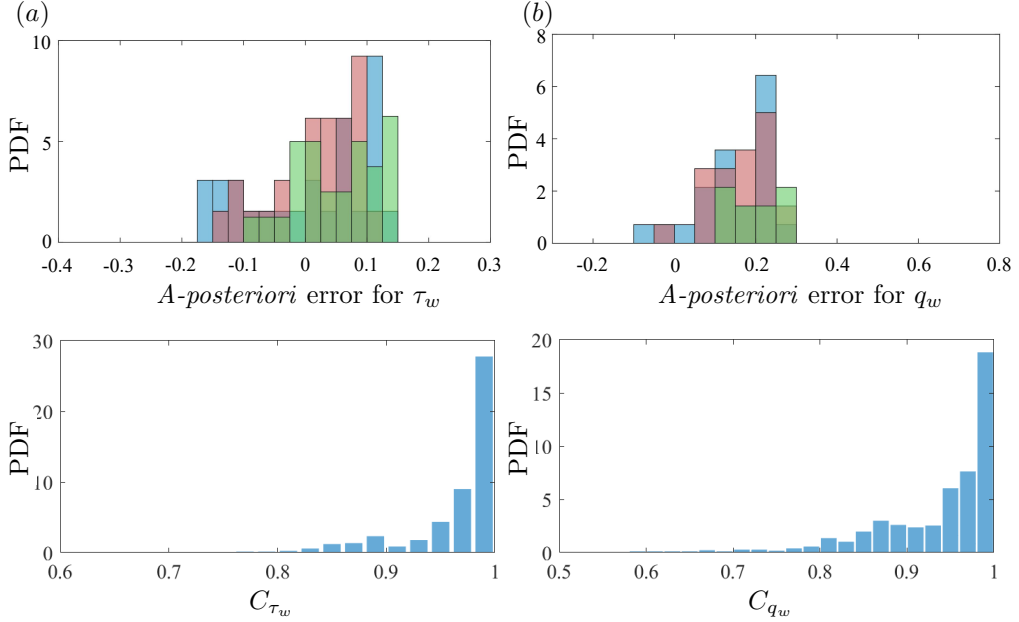


Figure 11: *A-posteriori* evaluation of BFWM-rough-v2 in WMLES of compressible turbulent channels. PDF of relative error for (a) wall shear stress and (b) wall heat flux along with their respective confidence scores below. Results are shown at three different grid resolutions: $\Delta/\delta = 1/20$ (blue), $1/10$ (red), and $1/5$ (green).

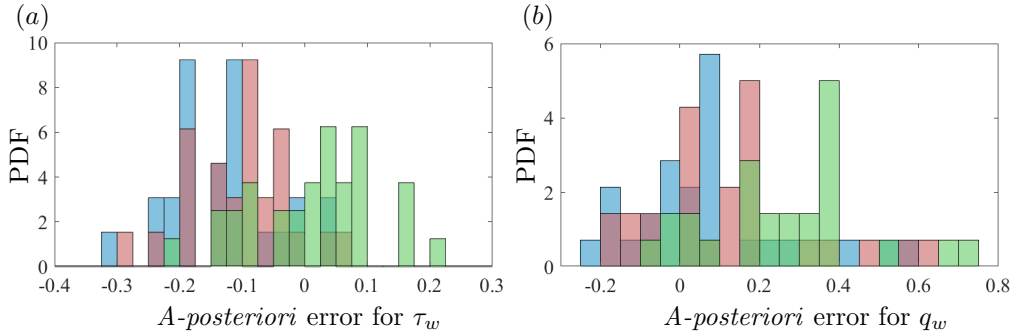


Figure 12: *A-posteriori* evaluation of EQWM- k_s in WMLES of compressible turbulent channels. PDFs of relative error for (a) wall shear stress and (b) wall heat flux. Results are shown at three different grid resolutions: $\Delta/\delta = 1/20$ (blue), $1/10$ (red), and $1/5$ (green).

BFWM-rough-v2, with the mean relative errors for τ_w and q_w are -7.60% and 19.30% , respectively. In particular, cases at high M_b exhibit significantly higher errors, with the wall heat flux results from EQWM- k_s reaching up to 80% . This indicates that the performance of EQWM- k_s deteriorates in supersonic flow regimes, where compressibility effects are strong, whereas BFWM-rough-v2 demonstrates superior predictive capability under these conditions.

The mean velocity and mean temperature profiles for a selection of test cases are shown in figure 13. The mean velocity profiles exhibit good agreement with DNS across different grid resolutions. In contrast, larger deviations are observed in the mean temperature profiles. Given that the *a-priori* results demonstrated stronger performance of BFWM-rough-v2, this discrepancy suggests that the observed errors in temperature are primarily due to external errors from the SGS model.

4.2 HPT blade with roughness

The high-pressure turbine (HPT) blade with a rough surface represents a challenging validation scenario due to its complex geometry and the presence of multiple flow phenomena, including strong pressure gradient effects, laminar–turbulent transition, and shock waves. Here, we use as reference case the DNS by Nardini *et al.* (2024), conducted under engine-relevant conditions with an exit Reynolds number of $Re_{exit} = 590,000$ based on the axial chord C_{ax} , and an exit Mach number of $M_{exit} = 0.9$. The rough

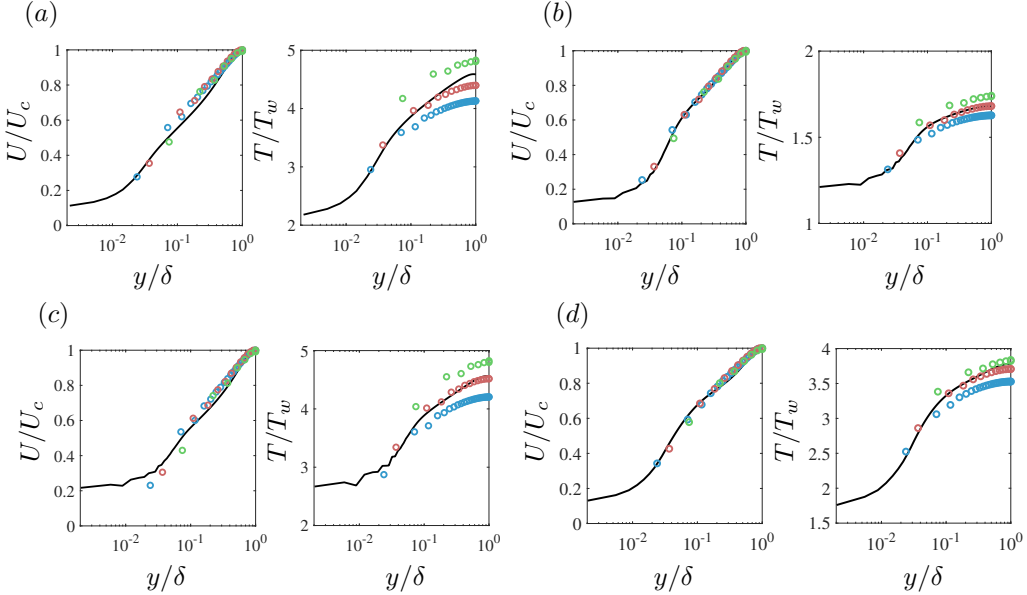


Figure 13: *A-posteriori* evaluation of BFWM-rough-v2 in WMLES of compressible turbulent channels. Mean velocity and mean temperature profiles for DNS (line) and WMLES (symbols). (a) GS1 at $M_b = 3.3$ and $Re_b = 15500$; (b) GS12 at $M_b = 1.7$ and $Re_b = 15500$; (c) GS13 at $M_b = 3.3$ and $Re_b = 15500$; (d) GS15 at $M_b = 3.3$ and $Re_b = 10000$. Results are shown at three different grid resolutions: $\Delta/\delta = 1/20$ (blue), $1/10$ (red), and $1/5$ (green).

Case	k_{rms}/C_{ax}	R_a/C_{ax}	S_k	K_u	ES
k_3^s	0.60×10^{-3}	0.48×10^{-3}	0.0	3.0	0.18

Table 4: The key geometrical roughness parameters of the blade surface roughness k_3^s from Nardini *et al.* (2024).

surface considered on the blade corresponds to the rough case k_3^s in Nardini *et al.* (2024). It consists of a Gaussian roughness representative of the surface texture associated with in-service degradation.

We carried out WMLES with BFWM-rough-v2 and EQWM- k_s . An illustration of the simulation setup and flow field is shown in figure 14(a). The spanwise domain is $0.4C_{ax}$ to ensure that the largest structures develop correctly. The turbulence intensity is set to 8% by adjusting the distance of the bars upstream of the blade. The Voronoi grids are generated with a background grid size of $\Delta_b = 0.0311C_{ax}$. The grids near the upstream bars are refined to $\Delta_b/2$ with 20 layers, and the flow near the bars is wall-resolved. The grids near the blade are refined by 4 levels, with each level reducing the grid size by 50% and adding 30 layers. With this mesh, the blade boundary layer is resolved by approximately 0 to 30 control volumes, with near-zero values occurring at the leading edge. The roughness sample tile is visualized in figure 14(b), and the key roughness parameters in Table 4 are extracted from the sample tile and used as input information for BFWM-rough-v2.

Figures 15(a) and (b) show the skin friction coefficient C_f and the wall heat flux Q along the axial position of the blade for WMLES using BFWM-rough-v2 and EQWM- k_s . Following Nardini *et al.* (2024), the skin friction coefficient is defined as $C_f = 2\tau_w/(\rho_{in}U_{in}^2)$, and the wall heat flux is defined as $Q = q_w T_{in}/U_{in}^2$, where subscript *in* denotes quantities at the inlet. For EQWM- k_s , the equivalent sand-grain roughness height is expressed as $k_s = Ak_{rms}$, where A is a constant scaling factor. Although Hama (1954) originally proposed $A = 5$ for Gaussian roughness surfaces, this value is not universally applicable, as other roughness characteristics, such as ES , can also influence the value of A . In our DNS database, the value of A varies considerably, ranging from 3.5 to 6.5 for Gaussian roughness surfaces. This variability introduces uncertainty in the estimation of k_s . To account for this, the EQWM- k_s model is evaluated over an extended range of $A = 3\text{--}7$.

The WMLES results are compared to the DNS from Nardini *et al.* (2024). Both BFWM-rough-v2 and EQWM- k_s capture the overall trends of C_f and Q on both the suction side (SS) and pressure side (PS) of the blade. However, the uncertainty in k_s introduces a pronounced deviation in EQWM- k_s predictions of C_f and Q within $0.5 < x/C_{ax} < 0.8$, where BFWM-rough-v2 demonstrates better predictive accuracy. In

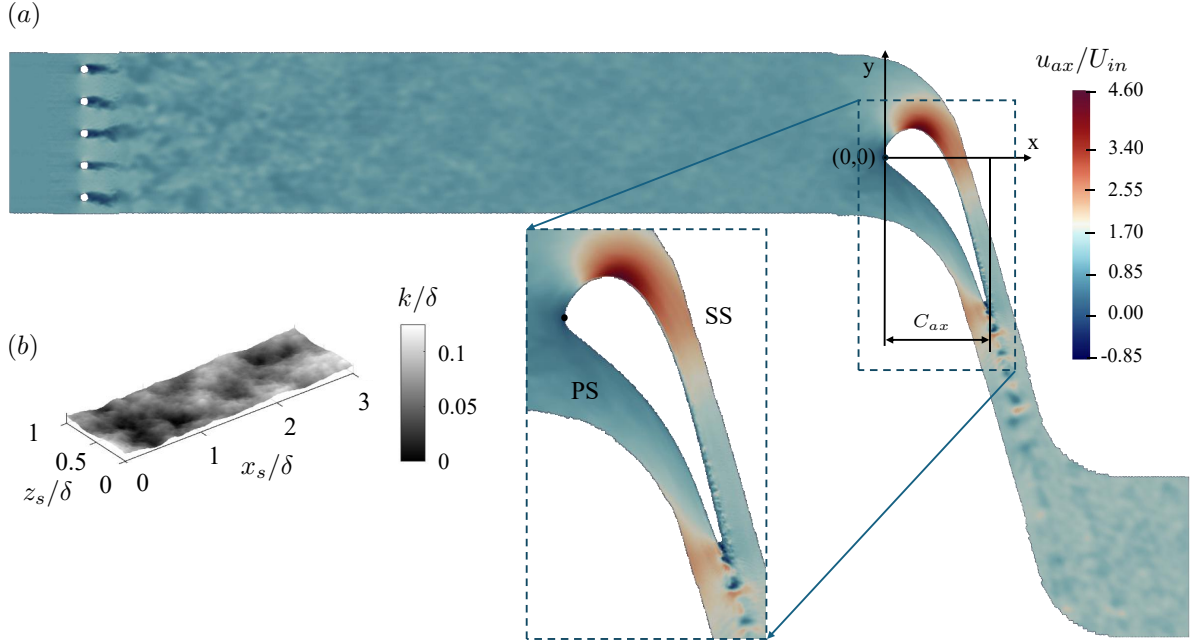


Figure 14: *A-posteriori* evaluation of BFWM-rough-v2 in WMLES of an HPT blade. (a) Visualization of the computational setup and instantaneous streamwise velocity field from the WMLES of HPT blade. The suction side of the blade is denoted by SS, while the pressure side is denoted by PS; (b) Rough surface tile corresponding to case k_3^s in Nardini *et al.* (2024).

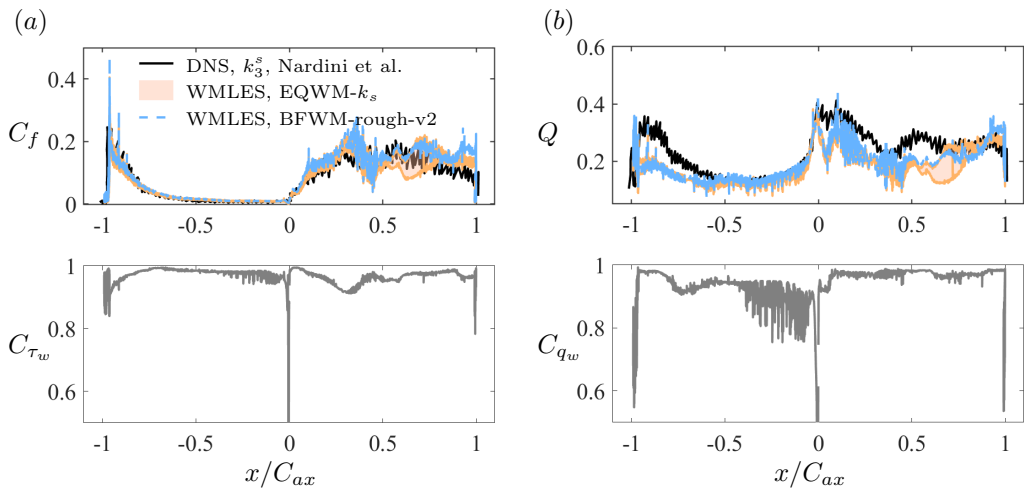


Figure 15: *A-posteriori* evaluation of BFWM-rough-v2 and EQWM- k_s in WMLES of an HPT blade. (a) Time and spanwise-averaged skin friction coefficient C_f and (b) time and spanwise-averaged wall heat flux Q along the axial position of the blade normalized by axial chord length x/C_{ax} . The time and spanwise-averaged confidence score for the prediction of C_f and Q is presented at the bottom line. The DNS results are from Nardini *et al.* (2024). The shaded area denotes the WMLES with EQWM- k_s , where $k_s = Ak_{rms}$, and $A = 3 \sim 7$. Note that $x/C_{ax} > 0$ and $x/C_{ax} < 0$ correspond to the SS and PS, respectively, with $x/C_{ax} = 0$ locate at the leading edge of the blade.

Case	No. of elements	k_{rms} (mm)	R_a (mm)	k_{rms}/R_a	ES	k_s (mm)
SG1	800	0.022	0.0186	1.183	0.12	0.30
SG2	600	0.020	0.0175	1.143	0.11	0.25
SG3	1000	0.024	0.0203	1.182	0.13	0.35

Table 5: The key roughness parameters of sand-grain roughness SG1, SG2, and SG3.

this region, roughness-induced normal shock waves give rise to complex interactions among shock-induced vortices, separation bubbles, and the boundary layer. On the PS, both wall models underpredict Q near the trailing edge, while on the SS, the underprediction extends over $0 < x/C_{ax} < 0.8$, where transition occurs.

In terms of confidence score, the predictions are generally associated with high values (typically above 0.9). Some exceptions occur near the stagnation point at the leading edge, where the first few points exhibit near-zero confidence. The former could be due to lack of grid points at the thin leading edge boundary layer whereas the latter could be associated to the strong curvature effects. While the confidence levels for Q are comparable to those for C_f , the prediction errors in Q are slightly larger in some regions. This discrepancy may reflect that, even when the model encounters inputs similar to those in the training set (and therefore assigns high confidence), the current building-block flows do not fully capture the complex physics of the HPT blade. In addition, the observed errors may be affected by limitations of the SGS model, or by a combination of both factors.

4.3 Hypersonic compression ramp with surface roughness

We evaluate the model in a hypersonic compression ramp with surface roughness. This configuration is relevant to high-speed entry vehicles, particularly for understanding the aerothermal loads on control surfaces at high flap angles, including surface heating and pressure forces during atmospheric entry. The setup, illustrated in Figure 16(a), follows the experimental configuration of Prince *et al.* (2005). The ramp angle is 30° , and the roughness was found to significantly influence peak heating and pressure at high flap angles ($\alpha_f \geq 30^\circ$). The free-stream Mach number is $M_\infty = 8.2$ and the flow occurs under low-enthalpy conditions, with no chemical reactions involved. The Reynolds number is $Re = 1.44 \times 10^6$, based on the distance from the leading edge to the flap hinge and free-stream conditions, denoted by L . Surface roughness is introduced by applying sandpaper to both the plate and flap surfaces.

For WMLES, a uniform velocity profile is imposed at the inflow boundary, while a sponge layer is applied at the outlet. Periodic boundary conditions are used in the spanwise direction. The farfield grid spacing is uniform with $\Delta = 0.1L$. Near the solid surfaces, mesh refinement is applied using seven successive levels, each reducing the grid spacing by 50%, resulting in approximately 30 grid points across the boundary layer at the flap hinge. Additionally, a refinement zone with constant spacing $\Delta \approx 30 \times 10^{-4}L$ is applied above both the plate and the ramp to accurately resolve the separation shock wave, reattachment shock wave, and the shock wave originating from the leading edge. In the simulations, a synthetic sand-grain rough surface labeled ‘SG1’ is generated to match the experimentally reported equivalent sand-grain roughness height of $k_s = 0.3$ mm. To evaluate the sensitivity of wall heat flux to variations in roughness, two additional surfaces (‘SG2’ and ‘SG3’) are constructed by adjusting the number of sand-grain elements to achieve $k_s = 0.25$ mm and $k_s = 0.35$ mm, respectively. A summary of the roughness characteristics is provided in Table 5, and a visualization of the flow field and rough surfaces is shown in figure 16.

Figure 17 presents the flow dynamics of the shock–boundary layer interaction at the compression corner, together with the heat transfer coefficient and the confidence score along the streamwise direction. The heat transfer coefficient is defined as $C_H = q_w/(\rho_\infty U_\infty C_p(T_w - T_r))$, where T_r is the recovery temperature. Upstream of the ramp, the heat transfer levels remain low, and both BFWM-rough-v2 and EQWM- k_s predict these values with reasonable accuracy. In this region, however, the model exhibits only moderate confidence, with scores around 0.5. This reduced confidence likely reflects the departure of the flow from a quasi-equilibrium boundary-layer state due to strong adverse pressure gradients, which drive the formation of a separated shear layer and a recirculation bubble. Such separation-induced dynamics lie outside the equilibrium assumptions of BFWM-rough-v2, reducing the reliability of the predictions despite the agreement in heat transfer levels.

At the reattachment point, the separated shear layer impinges on the wall and produces a reattachment shock that compresses the flow. The shear layer impingement and the reattachment shock inject a large amount of momentum and energy into the near-wall region, resulting in excessive energy transfer to the wall and giving rise to the heat flux overshoot phenomenon, where the wall heat flux spikes and exceeds the theoretical inviscid level. The WMLES results show that the BFWM-rough-v2 model predictions

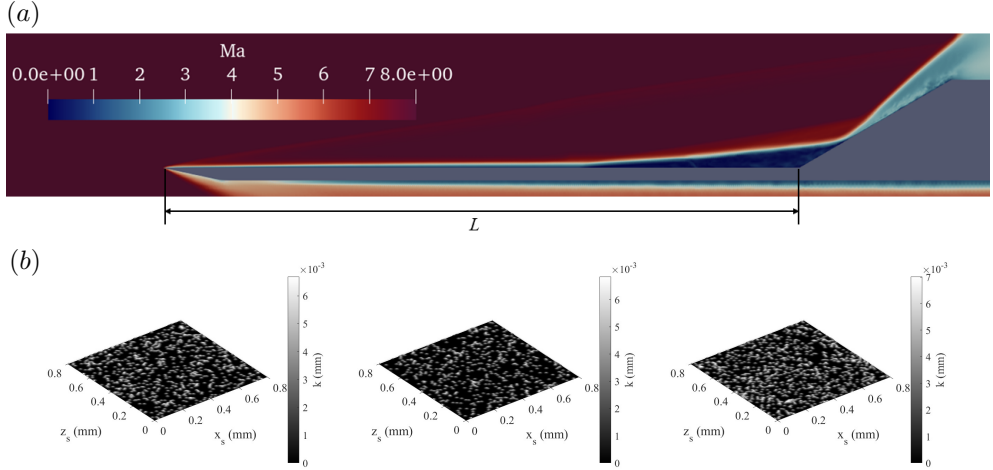


Figure 16: *A-posteriori* evaluation of BFWM-rough-v2 in WMLES of a hypersonic compression ramp. (a) Flow field over the compression ramp visualized by the contour plot of instantaneous Mach number. (b) The roughness tiles of sand-grain roughness, SG1 (left), SG2 (middle), and SG3 (right) corresponding to the roughness in Prince *et al.* (2005). The contour plot shows the surface elevation of the roughness, with units in millimeters.

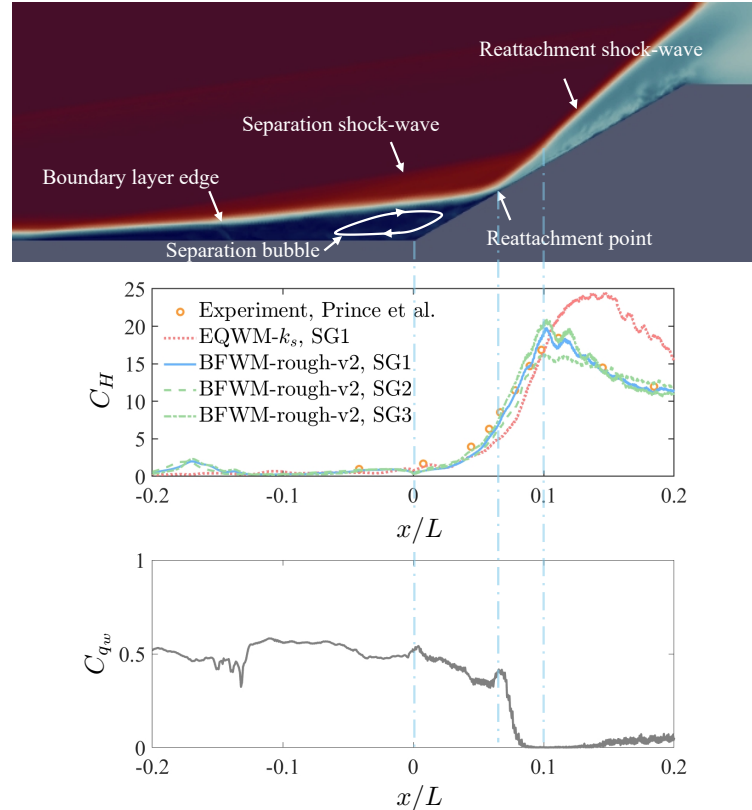


Figure 17: *A-posteriori* evaluation of BFWM-rough-v2 and EQWM- k_s in WMLES of a hypersonic compression ramp. The top panel illustrates the shock-boundary-layer interaction at the compression corner. The middle panel shows the wall heat transfer coefficient along the surface, comparing WMLES predictions using BFWM-rough-v2 (lines) and EQWM- k_s (dots) with experimental data from Prince *et al.* (2005) (symbols). The bottom panel displays the corresponding time and spanwise-averaged confidence score. The origin corresponds to the start of the ramp flap.

Re_∞ (1/ft)	M_∞	T_∞ (K)	P_∞ (Pa)	ρ_∞ (kg/m ³)	U_∞ (m/s)	h_{FR} (kg/m ² /s)
3.03×10^6	5.99	62.5	844.1	4.708×10^{-2}	948.7	2.163×10^{-1}
5.04×10^6	6.02	63.2	1421.0	7.843×10^{-2}	957.5	2.213×10^{-1}
8.34×10^6	6.03	58.6	2090.8	1.249×10^{-1}	918.1	3.407×10^{-1}

Table 6: Test conditions for the hemisphere model, corresponding to the experiment conditions for LaRC 20-Inch Mach 6 air tunnel Test 6975 in Hollis (2014).

Case	Element	Diam. (mm)	Diam. (inch)	k_s (inch)	k_{rms}/R_a	ES
20-Mesh	hemispherical	0.8530	0.0336	0.0168	1.156	0.330

Table 7: The key roughness parameters of 20-Mesh sand-grain roughness.

align well with the experimental data from Prince *et al.* (2005), capturing the sharp rise in heat flux at the ramp induced by surface roughness. The results also indicate that roughness density variation has minimal impact on the overall distribution of C_H , affecting only the peak values. In contrast, EQWM- k_s overpredicts the heating on the ramp by approximately 60% and incorrectly predicts the peak further downstream.

Finally, we observe that the confidence drops almost to zero at the location where the heat flux overshoot occurs. This behavior is attributed to the fact that the local flow inputs in this region lie outside the range represented in the training data. As shown in figure 16, the boundary layer downstream of the reattachment point becomes supersonic, with a peak Mach number at the matching location of $M_m \approx 2.6$, whereas the maximum value in the training dataset is $M_m \approx 0.7$. It is important to note that low confidence does not necessarily imply inaccurate predictions. Rather, it indicates that the model is operating in an extrapolative regime. Accurate predictions may still be obtained under extrapolation if the model captures the correct dimensionless scaling of the problem, as is the case here with M_m . Nonetheless, the likelihood of model underperformance increases in low-confidence regions, and such areas should be carefully inspected to identify potential issues.

4.4 Hypersonic blunt body with surface roughness

The last case considered is a blunt body with surface roughness. This case is relevant to EDL vehicles with ablated surfaces. The experimental data are obtained from NASA Langley Research Center's 20-Inch Mach 6 Air Tunnel (Hollis, 2014). The test model features a hemispherical nose with sand-grain roughness, and the physical radius of the body is $R_B = 0.0762$ m. Validation is performed against the "20-Mesh" roughness case reported in Hollis (2014), where the roughness height in viscous units, k^+ , ranges from 50 to 200. The sand-grain roughness on the model is created by applying an adhesive layer to a bed of uniformly manufactured spherical glass particles. For this problem, the flow over the hemisphere with a smooth surface remains laminar, whereas the presence of roughness triggers early transition and the development of a turbulent boundary layer on the hemisphere surface. Specifically, transition is initiated near the stagnation point. Three cases at different Reynolds numbers (per unit length) are considered, and the corresponding flow conditions are summarized in Table 6. The flow takes place under low-enthalpy conditions, with no chemical reactions involved.

For WMLES, the freestream velocity, pressure, and temperature are prescribed at the inflow and lateral boundaries (y and z directions). To suppress spurious acoustic reflections, a characteristic boundary condition with a damping (sponge) region is imposed near the outflow. The computational grid employs a Voronoi mesh with a base grid size of $\Delta = 0.6R_B$. Near the hemispherical surface, the grid is locally refined over 10 levels, halving the grid size at each level, to achieve approximately six control volumes across the boundary layer at $x/R_B = 0.4$. Additionally, a 5-level refinement region is applied around the shock wave to improve resolution in those areas. Figure 18(a) displays the configuration setup and the temperature field obtained from the WMLES for one case.

To obtain the roughness parameters required as input for BFWM-rough-v2, a synthetic roughness tile representative of the 20-Mesh case from Hollis (2014) is generated by randomly placing hemispherical elements on a flat substrate. The diameter of each hemispherical element is set to $D_s = 0.0336$ in, consistent with the experimental setup. The number of elements is adjusted to replicate both the roughness density observed in the experimental roughness tile and the equivalent sand-grain roughness height of $k_s = 0.0168$ inches. An example of the resulting surface is shown in Figure 18(b). The key roughness parameters are summarized in Table 7.

The instantaneous and time-azimuthally-averaged heat transfer predicted by WMLES with BFWM-rough-v2 and EQWM- k_s are shown in Figure 19, along with experimental measurements for a 20-Mesh rough surface under three test conditions. The heat transfer coefficient h is normalized by the theoretical

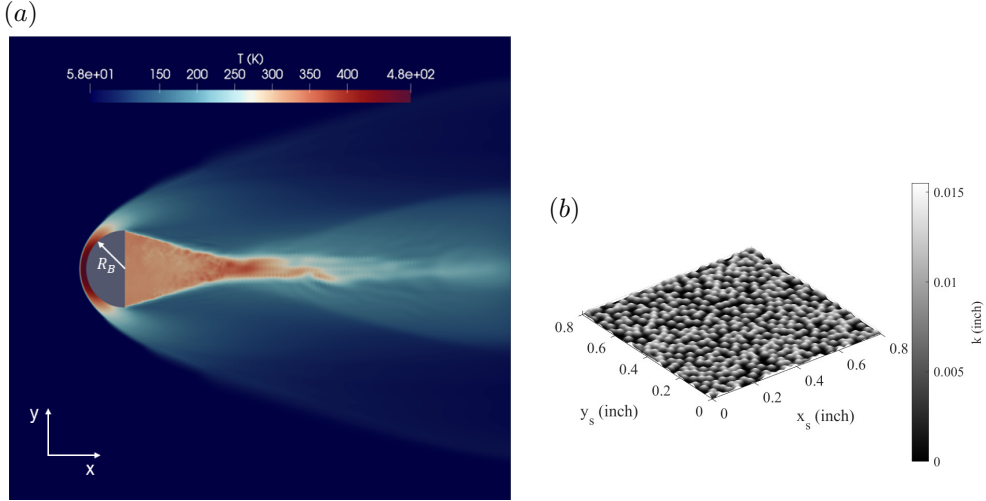


Figure 18: *A-posteriori* evaluation of BFWM-rough-v2 in WMLES of a hypersonic blunt body. (a) Instantaneous flow field for WMLES of hemisphere with 20-Mesh sand-grain roughness at Mach 6 across a free stream Reynolds number $Re_\infty = 8.34 \times 10^6/\text{ft}$. The contour shows the temperature variation at the plane $z = 0$. (b) A representative tile of randomly distributed sand-grain roughness, corresponding to the 20-Mesh roughness layout provided in Hollis (2014). The contour plot illustrates the surface elevation of the roughness, with units in inches.

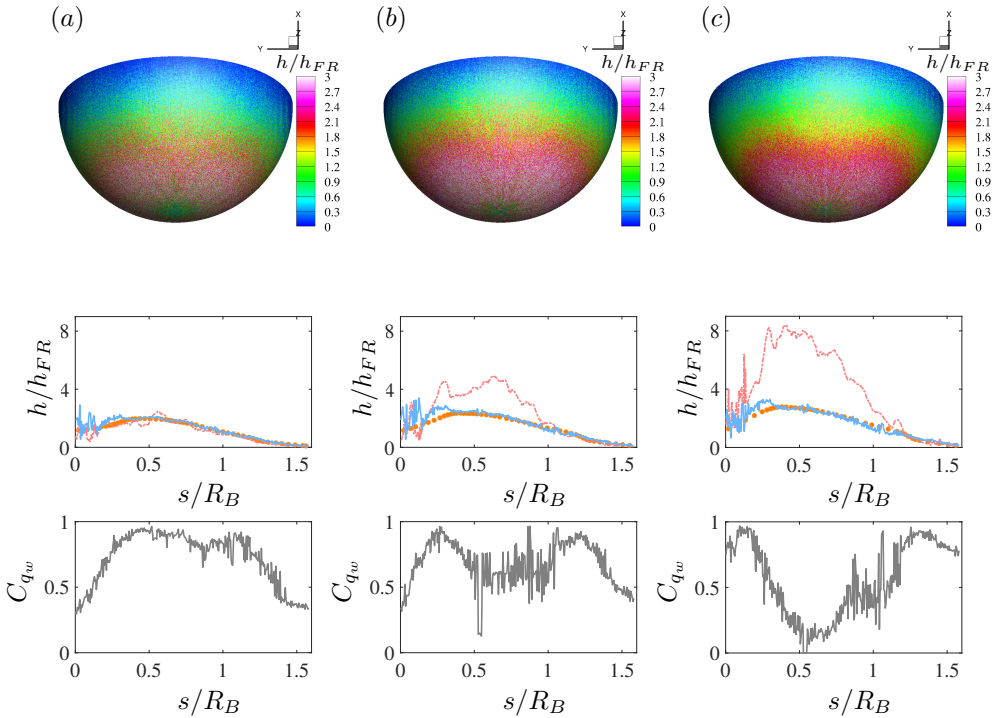


Figure 19: *A-posteriori* evaluation of BFWM-rough-v2 and EQWM- k_s in WMLES of a hypersonic blunt body. WMLES results using BFWM-rough-v2 for the 20-Mesh case (blue solid) are compared against experimental data from Hollis (2014) (orange dot) and WMLES with EQWM- k_s (red dash dot) at three different Reynolds numbers (per unit length): (a) $Re_\infty = 3.0 \times 10^6/\text{ft}$; (b) $Re_\infty = 5.0 \times 10^6/\text{ft}$; (c) $Re_\infty = 8.3 \times 10^6/\text{ft}$. Top panels: instantaneous heat transfer distribution on the hemisphere surface in terms of the normalized film coefficient, h/h_{FR} , where h is the heat-transfer film coefficient and h_{FR} is the theoretical prediction based on Fay–Riddell theory (Fay & Riddell, 1958). Middle and bottom panels: time- and azimuthally-averaged wall heat transfer and confidence score along the surface of the hemisphere from the front stagnation point to the trailing edge, covering the arc length (s) from $s = 0$ to one-quarter of the circumference.

reference value h_{FR} . The theoretical value h_{FR} is computed from the equilibrium stagnation-point boundary layer theory, as described by the correlation formula in Fay & Riddell (1958), with further details provided in Appendix E. The specific values of h_{FR} for each test condition are reported in Hollis (2017).

The results show that BFWM-rough-v2 captures the enhanced level of heat transfer due to surface roughness across different test conditions, closely matching the experimental data. The oscillations and overprediction for $s/R_B < 0.4$, where s is the arc length from the stagnation point, may be linked to the under-resolution of the thin boundary layer in WMLES. We observe relatively low confidence near the front stagnation region ($s/R_B < 0.3$) and the trailing edge ($s/R_B > 1.2$), possibly because strong pressure gradient and curvature effects reduce the validity of the model in these areas. Interestingly, the confidence in the mid-arc region ($0.3 < s/R_B < 1.2$) decreases with increasing Re_∞ , indicating that higher Re_∞ pushes the local inputs farther from what the model learned during training. We find that this is caused by the Reynolds number at the matching location Re_m exceeding the range represented in the training dataset at high Re_∞ .

In contrast, the WMLES with EQWM- k_s yields accurate predictions for $Re_\infty = 3.0 \times 10^6/\text{ft}$, but fails to do so for the two higher Reynolds numbers. In those cases, it overpredicts the heating augmentation by approximately 60% at $Re_\infty = 5.0 \times 10^6/\text{ft}$ and 120% at $Re_\infty = 8.3 \times 10^6/\text{ft}$ in the region $0.2 < s/R_B < 1$. This overprediction of wall heating may arise from the application of k_s correlations calibrated for low-speed turbulent boundary layers, which may not reliably extend to the flow conditions near the hemispherical surface. Additionally, the temperature log law used in EQWM- k_s may be insufficient to capture the temperature transport dynamics in this complex flow scenario.

5 Conclusions

We have developed a wall model for low- and high-speed turbulent flows that accounts for irregular subgrid-scale roughness features. The model is capable of predicting both wall shear stress and wall heat flux across a broad range of flow regimes, along with a confidence score in the predictions. The approach, implemented using artificial neural networks, is based on the building-block flow assumption (Lozano-Durán & Bae, 2023) and constitutes the second version of our earlier model for incompressible flows, *BFWM-rough*, introduced in Ma & Lozano-Durán (2025). The new model, referred to as *BFWM-rough-v2*, improves upon its predecessor by incorporating a revised input formulation, a new approach for confidence score estimation, a richer training database, and expanded applicability for WMLES of rough-wall flows.

To train the model, we constructed a DNS roughness database comprising both incompressible and compressible turbulent channel flows over irregular rough surfaces. The database includes 192 incompressible rough cases and 180 compressible rough cases spanning subsonic to supersonic flow regimes. The mean flow state, obtained via time and spatial averaging in the wall normal range $0.02 < y/\delta < 0.15$, is extracted from the DNS and used as input to the wall model. These mean-flow quantities, combined with statistical roughness parameters, are used to construct dimensionless input variables for the model. To identify the most predictive set of inputs, we apply dimensionless learning based on information-theoretic principles from Yuan & Lozano-Durán (2025). The resulting optimized wall model achieves L_2 prediction errors of 4.07% for wall shear stress and 2.89% for wall heat flux.

The model also incorporates a confidence score to assess the reliability of predictions under unseen flow conditions. This is implemented using a Spectral-normalized Neural Gaussian Process, which combines spectral-normalized hidden representations with a random-Fourier-feature Gaussian process layer. This approach yields calibrated predictive distributions that capture epistemic uncertainty, enabling the evaluation of the confidence in the predictions of the wall model.

We have validated BFWM-rough-v2 extensively across a wide range of flow conditions. The first validation is performed in canonical turbulent channel flows. WMLES of unseen incompressible and compressible turbulent channel flows are conducted, comprising a total of 78 incompressible and 84 compressible cases across various grid resolutions. The predicted frictional drag exhibits errors primarily within 10%, while heat flux predictions are mostly within 15%. The PDF of confidence scores indicates high model confidence ($0.8 \leq C \leq 1$) for the majority of test cases. The results also reveal that wall heat flux predictions are generally more sensitive to grid resolution and prone to larger errors compared to wall shear stress. For comparison, WMLES using an equilibrium-based wall model with prescribed k_s (EQWM- k_s) was also performed. While EQWM- k_s achieves wall shear stress predictions within 5% in incompressible channel flows, its accuracy significantly deteriorates in compressible flows, where errors in wall shear and wall heat flux can reach up to 30% and 80%, respectively, substantially higher than those observed with BFWM-rough-v2.

We have also validated BFWM-rough-v2 in more practical flow scenarios. The first such case is a

transonic HPT blade with Gaussian roughness. BFWM-rough-v2 demonstrates good predictive accuracy for the skin friction coefficient and outperforms EQWM- k_s in this regard. The model also captures the overall variation of wall heat flux along both the suction and pressure sides of the blade. However, it underpredicts the heat flux near the trailing edge on the pressure side, as well as in regions where normal shock waves are induced by the surface roughness. The confidence score of the model for the HPT blade is generally high ($C > 0.9$), suggesting that the local flow conditions are similar to those represented in the training dataset.

The next validation case involved a high-speed turbulent compression ramp with sandpaper roughness. BFWM-rough-v2 predictions show agreement within 5% with experimental measurements of wall heat transfer, while EQWM- k_s overpredicts the peak heating by approximately 60% and shifts the location of the peak further downstream. Although BFWM-rough-v2 successfully captures the enhancement in wall heat transfer, it exhibits moderate confidence ($C \approx 0.5$) upstream of the reattachment location and nearly zero confidence downstream. The reduced confidence upstream is likely due to flow separation at the ramp corner. The near-zero confidence downstream of reattachment is caused by the local near-wall flow becoming supersonic, which deviates substantially from the conditions represented in the training dataset.

Finally, we have performed WMLES of a blunt body with sand-grain roughness at $M_\infty = 6$ and three different Re_∞ . The BFWM-rough-v2 model accurately predicts the surface heating augmentation for $s/R_B \geq 0.4$, but tends to overpredict it for $s/R_B < 0.4$. This overprediction is attributed to limited resolution in the thin boundary layer near the front of the hemisphere. In contrast, EQWM- k_s increasingly overpredicts the heating augmentation as Re_∞ increases. Reduced confidence scores are observed near both the front and the trailing edge of the body, likely due to strong pressure-gradient and curvature effects. Furthermore, in the mid-arc region, the confidence of the model decreases with increasing Re_∞ , suggesting that higher Reynolds numbers amplify wall-heating gradients and shift the local input distribution further away from the training data.

Finally, we discuss the limitations of the model. In general, departures from the physical assumptions outlined in §3.2 lead to degraded model performance. Below, we summarize some of these key limitations. First, the model is trained primarily on canonical channel flows, which exhibit statistically stationary and fully developed turbulence. As a result, its ability to generalize to flows featuring strong pressure gradients, separation, reattachment, or shock-boundary-layer interactions is not guaranteed, as these regimes are not represented in the training dataset. Second, the training roughness, which includes Gaussian and Weibull surfaces, spans only a subset of possible roughness statistics, as they are isotropic and irregular. Engineering surfaces may exhibit anisotropy or possess roughness distributions that deviate substantially from the Gaussian or Weibull forms. Such conditions may lie outside the learned physics of the model, potentially leading to degraded or unreliable predictions. Third, the training data cover a limited range of Mach numbers (predominantly subsonic and supersonic). At higher Mach numbers, phenomena such as shock-induced heating and stronger temperature and density gradients may introduce physics not encountered during training, reducing reliability in hypersonic regimes. Last, when the model is deployed in WMLES, its performance depends on the choice of SGS model, since deficiencies in the latter can propagate into the wall-model inputs and lead to inaccurate predictions.

Our future work will focus on addressing the limitations discussed above and expanding the training database to encompass a broader range of flow conditions and roughness geometries. These efforts aim to further improve the overall performance and reliability of WMLES in complex, high-speed flow environments.

A Roughness parameter definition

The statistical roughness parameters are defined in table 8.

B Validation of DNS setup

The DNS performed in the present work has been validated by comparison with the reference DNS of Trettel & Larsson (2016). Table 9 summarizes the simulation details of both cases. Specifically, case M1.7R600 in Trettel & Larsson (2016) corresponds to our case M1.7-R15500. A grid convergence study was carried out for this case using three grid resolutions: ‘coarse’, ‘medium’, and ‘fine’. The results demonstrate that the ‘medium’ grid is sufficiently resolved, as it closely matches the ‘fine’ grid. For simplicity, we only present the results from the ‘medium’ in Figure 20. Good agreement is observed between our DNS and the reference, despite the fact that Trettel & Larsson (2016) employed a significantly larger domain size.

Mean height	$k_{avg} = \frac{1}{A_t} \int_{x,z} k(x, z) dA$
Crest height	$k_c = \max\{k(x, z)\} - \min\{k(x, z)\}$
Mean peak-to-valley height	$k_t = \text{mean}\{\max _{\delta \times \delta}\{k(x, z)\} - \min _{\delta \times \delta}\{k(x, z)\}\}$
Root-mean-square height	$k_{rms} = \sqrt{\frac{1}{A_t} \int_{x,z} (k(x, z) - k_{avg})^2 dA}$
First-order moment of height fluctuations	$R_a = \frac{1}{A_t} \int_{x,z} k(x, z) - k_{avg} dA$
Skewness	$S_k = \frac{1}{A_t k_{rms}^3} \int_{x,z} (k(x, z) - k_{avg})^3 dA$
Kurtosis	$K_u = \frac{1}{A_t k_{rms}^4} \int_{x,z} (k(x, z) - k_{avg})^4 dA$
Effective slope	$ES = \frac{1}{A_t} \int_{x,z} \left \frac{\partial k(x, z)}{\partial x} \right dA$
Surface porosity	$P_o = \frac{1}{A_t k_c} \int_0^{k_c} A_f(y) dy$
Frontal solidity	$\lambda_f = \frac{A_p}{A_t}$
Correlation length	$L_{cor} = \min_{\delta x} \{R_h(\delta x, 0) \leq 0.2\}$

Table 8: Definitions of roughness geometrical parameters. $k(x, z)$ is the roughness height function, and the reference $k = 0$ for the rough surface is defined at the minimum roughness height. $A_f(y)$ is the fluid area at the y location, A_p is the frontal projected area of the roughness elements, and A_t is the total plan area. The correlation lengths are computed as the horizontal separation at which the roughness height autocorrelation function $R_h(\delta x, \delta z) = \frac{1}{k_{rms}^2} \langle k(x + \delta x, z + \delta z) k(x, z) \rangle_{xz}$ drops below 0.2, where $\langle \cdot \rangle_{xz}$ denotes average over x and z . Given that the rough surfaces considered are isotropic, the parameters ES and L_{cor} are equivalent along any wall-parallel direction.

Case	$L_x \times L_y \times L_z$	M_b	Re_b	Re_τ	Re_τ^*	$-B_q$	Δx^+	Δy_{min}^+	Δy_{max}^+	Δz^+
Trettel & Larsson (2016)	$10\delta \times 2\delta \times 3\delta$	1.7	15500	972	596	0.05	10.85	0.87	7.97	6.07
M1.7-R15500	$3\delta \times 2\delta \times \delta$	1.7	15500	970	600	0.05	4.85	0.15	8.73	4.04
GS2-M1.7-R7500-minimal	$3\delta \times 2\delta \times \delta$	1.7	7500	706	430	0.042	5.30	0.10	5.96	4.41
GS2-M1.7-R7500-full	$6\delta \times 2\delta \times 3\delta$	1.7	7500	710	420	0.046	5.33	0.10	5.99	4.43

Table 9: Simulation details of the DNS validation cases for smooth- and rough-wall turbulent channel flows.

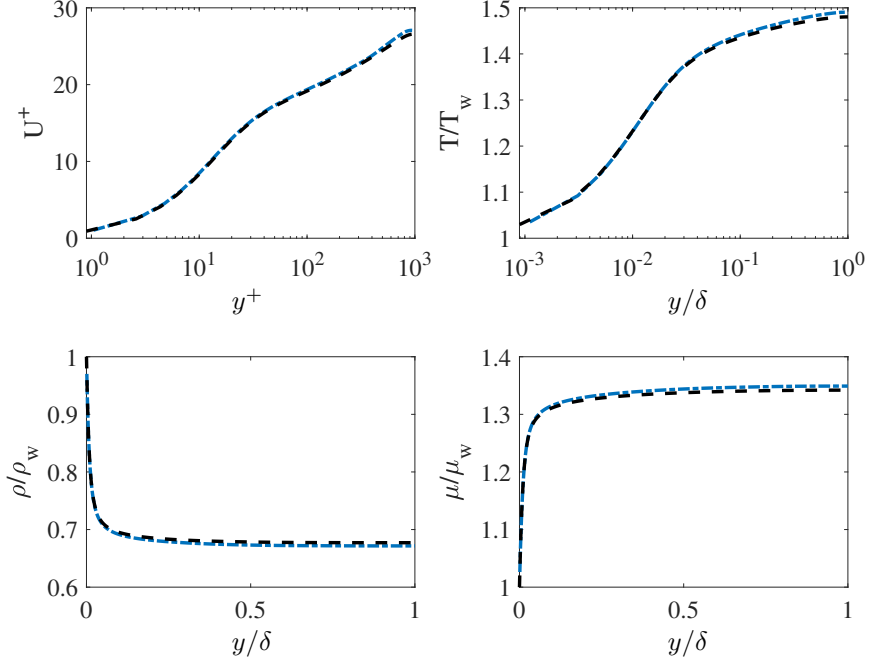


Figure 20: Validation for DNS of turbulent channel flow against Case M1.7R600 in Trettel & Larsson (2016): present (blue dot dash), Trettel & Larsson (2016) (black dash).

For rough-wall cases, a dedicated validation study was conducted to confirm the suitability of the minimal-span approach for wall model development. The selected roughness surface, GS2, features the largest roughness wavelength among all surfaces in the DNS database. As such, it provides the sparsest sampling of geometrical elements at this scale and represents the most challenging case for minimal-span modeling. A comparison is performed between a full-span channel ($6\delta \times 2\delta \times 3\delta$) and a minimal-span channel, both simulated under the same bulk Mach number M_b and bulk Reynolds number Re_b in the supersonic regime. The corresponding simulation parameters are provided in Table 9.

A comparison of mean velocity profiles is shown in Figure 21. Good agreement is observed in both Re_τ and $-B_q$, confirming the similarity between the two simulations. The mean velocity profiles are nearly identical, while the mean temperature and density profiles agree closely below $(y - d)/\delta = 0.05$, with deviations remaining within 3% beyond this region. Based on these results, the DNS mean data for $y/\delta < 0.15$ are considered reliable for wall-model training, with an estimated error below 3%.

C Mathematical formulation for a random-feature GP

The SNGP model is implemented as a residual-based deep neural network (DNN) consisting of two fully connected residual blocks, each containing 64 hidden units and employing ReLU activation functions. Each residual block is defined as $\mathbf{h}_l(\boldsymbol{\Pi}) = \boldsymbol{\Pi} + g_l(\boldsymbol{\Pi})$, where $\boldsymbol{\Pi} \in \mathbb{R}^d$ denotes the input vector to the l -th block and $\mathbf{h}_l(\boldsymbol{\Pi}) \in \mathbb{R}^d$ is the corresponding output vector. The residual mapping $g_l(\boldsymbol{\Pi})$ is given by $g_l(\boldsymbol{\Pi}) = a(W_l \boldsymbol{\Pi} + \mathbf{b}_l)$, where $W_l \in \mathbb{R}^{d \times d}$ and $\mathbf{b}_l \in \mathbb{R}^d$ denote the weight matrix and bias vector, respectively, and $a(\cdot)$ denotes the ReLU activation function applied element-wise. A final random-Fourier-feature Gaussian process layer is appended to the output to yield calibrated predictive distributions.

The SNGP is formulated by incorporating two key components into this residual DNN:

- (i) *Distance-preserving* hidden mapping via spectral normalization:

To ensure that the hidden mapping \mathbf{h} is distance preserving, it is sufficient to require each nonlinear residual block g_l to be α -Lipschitz continuous, that is,

$$\|g_l(\boldsymbol{\Pi}) - g_l(\boldsymbol{\Pi}')\|_{\mathcal{H}} \leq \alpha d_s(\boldsymbol{\Pi}, \boldsymbol{\Pi}'), \quad (9)$$

where $\boldsymbol{\Pi}, \boldsymbol{\Pi}' \in \mathbb{R}^d$ denote input vectors and $\|\cdot\|_{\mathcal{H}}$ denotes the norm in the hidden space.

Under this condition, the overall mapping \mathbf{h} of an L -layer residual network satisfies

$$L_1 d_s(\boldsymbol{\Pi}, \boldsymbol{\Pi}') \leq \|\mathbf{h}(\boldsymbol{\Pi}) - \mathbf{h}(\boldsymbol{\Pi}')\| \leq L_2 d_s(\boldsymbol{\Pi}, \boldsymbol{\Pi}'), \quad (10)$$

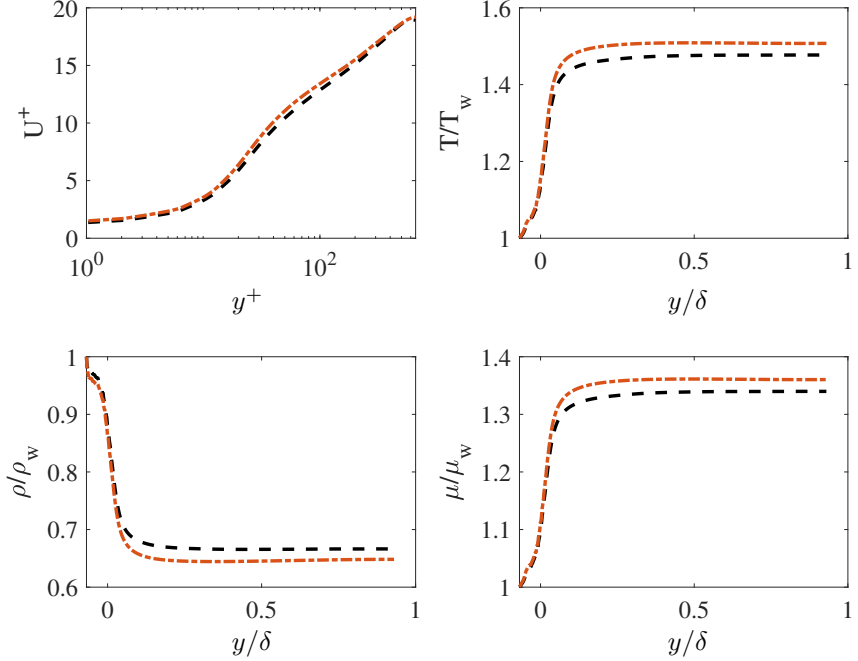


Figure 21: Comparison between DNS of rough-wall turbulent channel flow with a minimal-span (black dash) and a full-span (red dot dash) domain for Case GS2-M1.7-R7500.

where

$$L_1 = (1 - \alpha)^{L-1} \quad \text{and} \quad L_2 = (1 + \alpha)^{L-1}$$

represent the lower (contractivity) and upper (expansivity) bounds, respectively, for an L -layer residual network. The condition in Equation (9) can be satisfied by ensuring that the spectral norm of each weight matrix W_l is upper bounded. Specifically, since the residual mapping is given by $g_l(\boldsymbol{\Pi}) = a(W_l\boldsymbol{\Pi} + \mathbf{b}_l)$, its Lipschitz constant satisfies $\|g_l\|_{\text{Lip}} \leq \|W_l\boldsymbol{\Pi} + \mathbf{b}_l\|_{\text{Lip}} \leq \|W_l\|_2$ (Behrmann *et al.*, 2019). In this work, we enforce

$$W_l = \begin{cases} c W_l / \hat{\sigma}_l, & \text{if } \hat{\sigma}_l > c, \\ W_l, & \text{otherwise,} \end{cases} \quad (11)$$

where $\hat{\sigma}_l \approx \|W_l\|_2$ is estimated via power iteration and $c > 0$ is a tunable hyperparameter that is determined based on the validation data to specify the desired upper bound on the spectral norm.

(ii) *Distance awareness* through a random-feature GP layer:

The random Fourier feature method is employed to project the final hidden representation into a high-dimensional feature space. This method provides an efficient approximation to the kernel function and allows the subsequent probabilistic model to operate on a feature space that encodes non-linearities without requiring explicit kernel computations.

To enforce distance awareness, we adopt a Gaussian Process (GP) with a radial basis function (RBF) kernel, which is the classical model that satisfies this property (Rasmussen & Williams, 2006). Although the RBF kernel is used here for simplicity, the framework can be readily extended to other kernels by adjusting the activation function and random feature distribution.

Given a training dataset $\mathcal{D} = \{(\boldsymbol{\Pi}, \boldsymbol{\Pi}_o)\}$ with N data points, the hidden representation of the DNN for each training point is denoted as $h_i = h(\boldsymbol{\Pi}_i)$ where $i = 1, 2, \dots, N$, and the GP conditioned on the hidden representations is denoted as $\mathbf{g}_{N \times 1} = [g(h_1), \dots, g(h_N)]^\top$. The prior distribution of a GP model equipped with an RBF kernel is a multivariate normal distribution:

$$\mathbf{g}_{N \times 1} \sim \mathcal{N}(\mathbf{0}_{N \times 1}, m^2 \mathbf{K}_{N \times N}), \quad (12)$$

where m^2 is the kernel amplitude, and the RBF kernel is defined as:

$$\mathbf{K}_{ij} = \exp\left(-\frac{\|h_i - h_j\|_2^2}{2}\right). \quad (13)$$

However, computing the GP prior in Equation (12) is computationally expensive, as it requires the inversion of an $N \times N$ kernel matrix \mathbf{K} , which scales cubically with the number of samples, i.e., $\mathcal{O}(N^3)$. To deal with this challenge, the GP prior in Equation (12) is approximated by constructing a low-rank approximation of the kernel matrix $K = \Phi\Phi^\top$ using random Fourier features (Rahimi & Recht, 2007). This yields a random-feature Gaussian process:

$$g_{N \times 1} \sim \mathcal{N}(\mathbf{0}_{N \times 1}, \Phi\Phi^\top_{N \times N}), \quad \text{where } \Phi_{i, D_L \times 1} = \sqrt{\frac{2m^2}{D_L}} \cos(-\mathbf{W}_L h_i + \mathbf{b}_L). \quad (10)$$

Here, D_L is the number of random features. We tested $D_L = 512, 1024$ and 2048 and find that the model performance is not very sensitive to different values of D_L , and $D_L = 512$ is sufficient in our work. $\Phi_{i, D_L \times 1}$ is the final layer feature, where the random weights $\mathbf{W}_L \in \mathbb{R}^{D_L \times D_{L-1}}$ are drawn independently from $\mathcal{N}(0, I)$, and the bias term $\mathbf{b}_L \in \mathbb{R}^{D_L}$ is sampled independently from $\text{Uniform}(0, 2\pi)$.

Consequently, we replace the standard deterministic output layer with a Bayesian linear regression head. The GP prior can be expressed as a neural network layer with fixed hidden weights \mathbf{W}_L and learnable output weights β with a prior variance σ_p^2 :

$$g(h_i) = \Phi_{i, D_L \times 1}^\top \beta, \quad \text{with prior } \beta_{D_L \times 1} \sim \mathcal{N}(0, \sigma_p^2 I_{D_L \times D_L}). \quad (14)$$

By Bayes' rule, the posterior distribution of β is proportional to the likelihood times the prior:

$$p(g | \mathcal{D}) \propto p(\mathcal{D} | g) p(g), \quad (15)$$

where $p(g)$ denotes the GP prior (not to be confused with pressure). For a regression task, the data likelihood $p(\mathcal{D} | g)$ with an observation noise variance σ_n^2 can be modeled using the exponentiated squared loss:

$$p(\mathcal{D} | g) = \exp\left(-\frac{1}{2\sigma_n^2} \|\Pi_o - g\|_2^2\right). \quad (16)$$

Note that the observation noise variance σ_n^2 represents the variance of the residuals (i.e., the mismatch between the model predictions and the observed targets) in the training data. It is typically estimated once during training and then treated as a constant hyperparameter throughout the GP inference and prediction steps.

The negative log-posterior of the Bayesian linear regression head is given by

$$-\log p(g | \mathcal{D}) = \frac{1}{2\sigma_n^2} \|\Pi_o - \Phi\beta\|_2^2 + \frac{1}{2\sigma_p^2} \|\beta\|_2^2 + \text{const.} \quad (17)$$

In this equation, it can be observed that the prior variance σ_p^2 controls the strength of regularization and defines the initial uncertainty before seeing the data. A common default value $\sigma_p = 2$ is used in our work. By rearranging terms, the posterior distribution over the regression weights β can be expressed in closed form as a multivariate Gaussian:

$$p(\beta | \mathcal{D}) = \mathcal{N}(\mu_\beta, \Sigma_\beta), \quad \mu_\beta = \frac{1}{\sigma_n^2} \Sigma_\beta \Phi^\top \Pi_o, \quad \Sigma_\beta = \left(\frac{1}{\sigma_n^2} \Phi^\top \Phi + \frac{1}{\sigma_p^2} I\right)^{-1}. \quad (18)$$

For a new input $\mathbf{\Pi}_*$ with feature representation $\phi_* = \phi(\mathbf{h}_*)$, the predictive distribution is obtained by marginalizing over the posterior of β :

$$p(\Pi_{o*} | \mathbf{\Pi}_*, \mathcal{D}) = \mathcal{N}(\phi_*^\top \mu_\beta, \phi_*^\top \Sigma_\beta \phi_* + \sigma_n^2). \quad (19)$$

The predictive variance consists of two components:

$$\underbrace{\phi_*^\top \Sigma_\beta \phi_*}_{\text{epistemic uncertainty}} + \underbrace{\sigma_n^2}_{\text{aleatoric uncertainty}}.$$

The first term, $\sigma_e^2 = \phi_*^\top \Sigma_\beta \phi_*$, represents the *epistemic uncertainty*. It increases in regions far from the training data, reflecting the model's lack of knowledge and assessing the reliability of predictions in unseen or extrapolative regimes. The second term, σ_n^2 , corresponds to the *aleatoric uncertainty* caused by inherent observation noise and remains constant regardless of the data size. The epistemic uncertainty obtained from the SNGP model is therefore used to quantify the model uncertainty in this work.

D EQWM for rough walls with prescribed k_s

The EQWM- k_s provides an algebraic formulation based on the logarithmic law of the wall for both velocity and temperature, extended to account for surface roughness effects. It assumes a fully developed, equilibrium turbulent boundary layer characterized by a logarithmic profile.

For smooth walls, the log law is expressed as

$$U^+ = \frac{1}{\kappa_v} \ln(y^+) + 5, \quad (20)$$

where κ_v is the von Kármán constant. For rough walls, this relationship is modified to include the velocity deficit as

$$U^+ = \frac{1}{\kappa_v} \ln\left(\frac{y}{k_s}\right) + 8.5, \quad (21)$$

where k_s is the equivalent sand-grain roughness height. Consequently, the wall shear stress is obtained algebraically from the local velocity u_m and density ρ_m at the matching location y_m as

$$\tau_w = \rho_m \left[\frac{u_m}{\frac{1}{\kappa_v} \ln\left(\frac{y_m}{k_s}\right) + 8.5} \right]^2. \quad (22)$$

The temperature law of the wall provides an empirical relationship between the nondimensional temperature and wall-normal distance in turbulent boundary layers, analogous to the velocity log-law for momentum transfer (Kader, 1981; Bradshaw, 2013). The correction function T^* ensures a smooth transition from the linear sublayer to the logarithmic region and is defined as:

$$T^* = \begin{cases} 0.5 Re_m, & Re_m \leq y^* \\ \frac{0.5 y^{*2}}{Re_m} + C_t \left(1 - \frac{y^*}{Re_m}\right) + \frac{\ln(Re_m/y^*)}{\kappa_t}, & Re_m > y^* \end{cases} \quad (23)$$

where the Reynolds number $Re_m = \frac{\rho_m u_\tau y_m}{\mu_m}$, $\kappa_t = \frac{\kappa_v}{Pr_t}$, $Pr_t = 0.85$, $C_t = 3.9$, and $y^* = 8.28$ are empirical constants.

The algebraic wall model for wall heat flux is then derived by relating the mean temperature gradient at the matching location y_m to the wall heat flux through the total thermal conductivity λ_{tot} and the temperature law correction:

$$q_w = \frac{\lambda_{\text{tot}}(T_m - T_w)}{y_m [1 + \kappa_t T^*]}. \quad (24)$$

The term $[1 + \kappa_t T^*]$ acts as a turbulent diffusion damping factor that modulates the temperature gradient near the wall. The total thermal conductivity λ_{tot} includes both molecular and turbulent contributions,

$$\lambda_{\text{tot}} = \lambda + \lambda_t, \quad \lambda_t = \frac{\mu_t c_p}{Pr_t}, \quad (25)$$

where the eddy viscosity μ_t is obtained using a mixing-length model with near-wall damping (Kawai & Larsson, 2010) with $A^+ = 17$:

$$\mu_t = \kappa_v \rho y \sqrt{\frac{\tau_w}{\rho}} D, \quad D = 1 - \exp\left[-\left(\frac{y^+}{A^+}\right)^2\right], \quad (26)$$

where τ_w is obtained from Equation (22).

E Fay–Riddell stagnation-point heat-transfer theory

We follow previous works and use the Fay–Riddell stagnation-point heat-transfer theory (Fay & Riddell, 1958) to obtain a reference heat flux for the blunt body (Hollis, 2014; Cheatwood *et al.*, 2024). The theory provides a semi-empirical expression for the convective heat-transfer rate to a blunt body at the stagnation point under high-enthalpy, equilibrium-flow conditions. The model assumes a steady, axisymmetric, laminar boundary layer in chemical and thermal equilibrium between the post-shock flow and the wall. For an equilibrium laminar boundary layer with a Lewis number (ratio of thermal to mass diffusivity) of $Le = 0.71$, the stagnation-point convective heat flux is given by

$$q_q = 0.76 Pr^{-0.6} (\rho_w \mu_w)^{0.1} (\rho_e \mu_e)^{0.4} \left[1 + (Le^{0.52} - 1) (h_D/h_e)\right] (h_e - h_w) \sqrt{\left(\frac{du_e}{dx}\right)_s}, \quad (27)$$

where Pr is the Prandtl number, ρ and μ are the density and dynamic viscosity (subscripts w and e denote wall and boundary-layer-edge conditions), h_e and h_w are the static enthalpies at the boundary-layer edge and at the wall, h_D is the dissociation (diffusion) enthalpy scale, and $(du_e/dx)_s$ is the stagnation-point edge velocity gradient (often approximated using the nose radius R_n , edge pressure p_e , freestream pressure p_∞ , and edge density ρ_e).

Acknowledgements

We gratefully acknowledge Y. Yuan for the helpful discussion on dimensionless learning based on information. We also gratefully acknowledge M. Whitmore, A. Elnahhas, R. Agrawal, and G. Arranz for their contributions to the DNS compressible flow database. We thank C. Pederson for the insightful discussion on this work.

Funding

This work was supported by the National Science Foundation under Award Number 2317254 and by an Early Career Faculty grant from NASA's Space Technology Research Grants Program (Grant Number 80NSSC23K1498). The authors acknowledge ACCESS allocation and the Oak Ridge Leadership Computing Facility, which is a DOE Office of Science User Facility supported under Contract DE-AC05-00OR22725, for providing HPC resources that have contributed to the research results reported within this work.

Declaration of interests

The authors report no conflict of interest.

References

ARRANZ, G., LING, Y., COSTA, S., GOC, K. & LOZANO-DURÁN, A. 2024 Building-block-flow computational model for large-eddy simulation of external aerodynamic applications. *Commun. Eng.* **3**, 127.

BEHRMANN, J., GRATHWOHL, W., CHEN, R. T. Q., DUVENAUD, D. & JACOBSEN, J. 2019 Invertible residual networks. In *ICML*, pp. 573–582. PMLR.

BERNARDINI, M., PIROZZOLI, S. & ORLANDI, P. 2012 Compressibility effects on roughness-induced boundary layer transition. *Int. J. Heat Fluid Flow* **35**, 45–51.

BONS, J. P. 2010 A review of surface roughness effects in gas turbines. *J. Turbomach.* .

BOSE, S. T. & PARK, G. I. 2018 Wall-modeled large-eddy simulation for complex turbulent flows. *Annu. Rev. Fluid Mech.* **50**, 535–561.

BOWERSOX, R. 2007 Survey of high-speed rough wall boundary layers: invited presentation. In *AIAA Paper 2007-3998*.

BRADSHAW, P. 1977 Compressible turbulent shear layers. *Annu. Rev. Fluid Mech.* **9**, 33–52.

BRADSHAW, P. 2013 *An introduction to turbulence and its measurement: thermodynamics and fluid mechanics series*. Elsevier.

BRES, G. A., BOSE, S. T., EMORY, M., HAM, F. E., SCHMIDT, O. T., RIGAS, G. & COLONIUS, T. 2018 Large-eddy simulations of co-annular turbulent jet using a voronoi-based mesh generation framework. In *2018 AIAA/CEAS Aeroacoustics Conference*, p. 3302.

CABOT, W. & MOIN, P. 2000 Approximate wall boundary conditions in the large-eddy simulation of high reynolds number flow. *Flow Turbul. Combust.* **63** (1), 269–291.

CHEATWOOD, J., JOHNSTON, C. O. & HOLLIS, B. R. 2024 Mars sample return earth entry system woven roughness mach 6 aeroheating test. In *AIAA SciTech 2024 Forum*, p. 0443.

CHEN, P.E.S., Lv, Y., Xu, H.H.A., SHI, Y. & YANG, X.I.A. 2022 Les wall modeling for heat transfer at high speeds. *Phys. Rev. Fluids* **7** (1), 014608.

CHENG, C. & FU, L. 2024 A reynolds analogy model for compressible wall turbulence. *J. Fluid Mech.* **999**, A20.

CHUNG, D., CHAN, L., MACDONALD, M., HUTCHINS, N. & OOI, A. 2015 A fast direct numerical simulation method for characterising hydraulic roughness. *J. Fluid Mech.* **773**, 418–431.

CHUNG, D., HUTCHINS, N., SCHULTZ, M. P. & FLACK, K. A. 2021 Predicting the drag of rough surfaces. *Annu. Rev. Fluid Mech.* **53**, 439–471.

COLEMAN, G. N., KIM, J. & MOSER, R. D. 1995 A numerical study of turbulent supersonic isothermal-wall channel flow. *J. Fluid Mech.* **305**, 159–183.

COVER, T. M. 1999 *Elements of Information Theory*. John Wiley & Sons.

DIRLING, R. 1973 A method for computing roughwall heat transfer rates on reentry nosetips. In *AIAA Paper 1973-0763*.

EKOTO, I. W., BOWERSOX, R. D. W., BEUTNER, T. & GOSS, L. 2008 Supersonic boundary layers with periodic surface roughness. *AIAA J.* **46** (2), 486–497.

FAY, J. A. & RIDDELL, F. R. 1958 Theory of stagnation point heat transfer in dissociated air. *J. Aerosp. Sci.* **25**, 73–85.

FINSON, M. & CLARKE, A. 1980 The effect of surface roughness character on turbulent re-entry heating. In *AIAA Paper 1980-1459*.

FLACK, K. A. & SCHULTZ, M. P. 2010 Review of hydraulic roughness scales in the fully rough regime. *J. Fluids Eng.* .

FOROOGHİ, P., STROH, A., MAGAGNATO, F., JAKIRLIĆ, S. & FROHNAPFEL, B. 2017 Toward a universal roughness correlation. *J. Fluids Eng.* **139** (12), 121201.

FU, L., KARP, M., BOSE, S. T., MOIN, P. & URZAY, J. 2021 Shock-induced heating and transition to turbulence in a hypersonic boundary layer. *J. Fluid Mech.* **909**, A8.

GAITONDE, D. V. & ADLER, M. C. 2023 Dynamics of three-dimensional shock-wave/boundary-layer interactions. *Annu. Rev. Fluid Mech.* **55**, 291–321.

GARCÍA-MAYORAL, R., CHUNG, D., DURBIN, P., HUTCHINS, N., KNOPP, T., MCKEON, B. J., PIOMELLI, U. & SANDBERG, R. D. 2024 Challenges and perspective on the modelling of high-re, incompressible, non-equilibrium, rough-wall boundary layers. *J. Turbul.* **25** (10-11), 423–449.

GRiffin, K. P., FU, L. & MOIN, P. 2021 Velocity transformation for compressible wall-bounded turbulent flows with and without heat transfer. *Proc. Natl. Acad. Sci.* **118** (34), e2111144118.

GRiffin, K. P., FU, L. & MOIN, P. 2023 Near-wall model for compressible turbulent boundary layers based on an inverse velocity transformation. *J. Fluid Mech.* **970**, A36.

GUARINI, S. E., MOSER, R. D., SHARIFF, K. & WRAY, A. 2000 Direct numerical simulation of a supersonic turbulent boundary layer at mach 2.5. *J. Fluid Mech.* **414**, 1–33.

HAMA, F. R. 1954 Boundary layer characteristics for smooth and rough surfaces. *Trans. Soc. Nav. Arch. Marine Engrs.* **62**, 333–358.

HANSEN, N., MÜLLER, S. D. & KOUMOUTSAKOS, P. 2003 Reducing the time complexity of the derandomized evolution strategy with covariance matrix adaptation. *Evol. Comput.* **11**, 1–18.

HOLLIS, B. R. 2014 Distributed roughness effects on blunt-body transition and turbulent heating. In *AIAA Paper 2014-0238*.

HOLLIS, B. R. 2017 Experimental investigation of roughness effects on transition onset and turbulent heating augmentation on a hemisphere at mach 6 and mach 10. *Tech. Rep.* NASA TP-2017-219588. NASA Langley Research Center.

IYER, P. S. & MALIK, M. R. 2019 Analysis of the equilibrium wall model for high-speed turbulent flows. *Phys. Rev. Fluids* **4**, 074604.

JIMÉNEZ, J. 2004 Turbulent flows over rough walls. *Annu. Rev. Fluid Mech.* **36** (1), 173–196.

JIMÉNEZ, J. & MOIN, P. 1991 The minimal flow unit in near-wall turbulence. *J. Fluid Mech.* **225**, 213–240.

JOUYBARI, M. A., YUAN, J., LI, Z., BRERETON, G. J. & JABERI, F. A. 2023 Supersonic turbulent flows over sinusoidal rough walls. *J. Fluid Mech.* **956**, A3.

KADER, B. A. 1981 Temperature and concentration profiles in fully turbulent boundary layers. *Int. J. Heat Mass Transf.* **24** (9), 1541–1544.

KADIVAR, M. & GARG, H. 2025 Turbulent heat transfer over roughness: a comprehensive review of theories and turbulent flow structure. *Int. J. Thermofluid* **26**, 100967.

KADIVAR, M., TORMEY, D. & MCGRANAGHAN, G. 2021 A review on turbulent flow over rough surfaces: Fundamentals and theories. *Int. J. Thermofluid* **10**, 100077.

KAWAI, S. & LARSSON, J. 2010 A dynamic wall model for large-eddy simulation of high reynolds number compressible flows. *CTR Annual Research Briefs* pp. 25–37.

KEATING, A., PIOMELLI, U., BREMHORST, K. & NEŠIĆ, S. 2004 Large-eddy simulation of heat transfer downstream of a backward-facing step. *J. Turbul.* **5** (1), 020.

KRISTIADI, A., HEIN, M. & HENNIG, P. 2020 Being bayesian, even just a bit, fixes overconfidence in relu networks. In *ICML*, pp. 5436–5446. PMLR.

LARSSON, J., KAWAI, S., BODART, J. & BERMEJO-MORENO, I. 2016 Large eddy simulation with modeled wall-stress: recent progress and future directions. *Mech. Eng. Rev.* **3** (1), 15–00418.

LATIN, R. M. & BOWERSOX, R. D. W. 2000 Flow properties of a supersonic turbulent boundary layer with wall roughness. *AIAA J.* **38** (10), 1804–1821.

LATIN, R. M. & BOWERSOX, R. D. W. 2002 Temporal turbulent flow structure for supersonic rough-wall boundary layers. *AIAA J.* **40** (5), 832–841.

LEE, M. & MOSER, R. D. 2015 Direct numerical simulation of turbulent channel flow up to. *J. Fluid Mech.* **774**, 395–415.

LI, S., YANG, X. & LV, Y. 2022 Predictive capability of the logarithmic law for roughness-modeled large-eddy simulation of turbulent channel flows with rough walls. *Phys. Fluids* **34** (8), 085112.

LING, YUENONG, HAYAT, IMRAN, GOC, KONRAD & LOZANO-DURAN, ADRIAN 2025 General-purpose data-driven wall model for low-speed flows part i: Baseline model. *arXiv preprint arXiv:2511.16511* .

LIU, J. Z., PADHY, S., REN, J., LIN, Z., WEN, Y., JERFEL, G., NADO, Z., SNOEK, J., TRAN, D. & LAKSHMINARAYANAN, B. 2023 A simple approach to improve single-model deep uncertainty via distance-awareness. *J. Mach. Learn. Res.* **24** (42), 1–63.

LOZANO-DURÁN, ADRIÁN & BAE, HYUNJI JANE 2020 Self-critical machine-learning wall-modeled les for external aerodynamics. *CTR Annual Res. Briefs 2020* .

LOZANO-DURÁN, A. & BAE, H. J. 2023 Machine learning building-block-flow wall model for large-eddy simulation. *J. Fluid Mech.* **963**, A35.

MA, R., ALAMÉ, K. & MAHESH, K. 2021 Direct numerical simulation of turbulent channel flow over random rough surfaces. *J. Fluid Mech.* **908**, A40.

MA, R. & LOZANO-DURÁN, A. 2025 Machine-learning wall-model large-eddy simulation accounting for isotropic roughness under local equilibrium. *J. Fluid Mech.* **1007**, A17.

MA, R., YUAN, Y., ARRANZ, G., LING, Y., AGRAWAL, R., WHITMORE, M., ELNAHHAS, A., PEDERSON, C. & LOZANO-DURÁN, A. 2024 Building-block-flow model for les of high-speed flows. *Proceedings of the CTR Summer Program* pp. 385–394.

MACDONALD, M., CHUNG, D., HUTCHINS, N., CHAN, L., OOI, A. & GARCÍA-MAYORAL, R. 2017 The minimal-span channel for rough-wall turbulent flows. *J. Fluid Mech.* **816**, 5–42.

METTU, B. R. & SUBBAREDDY, P. K. 2022 Wall-modeled large eddy simulation of high speed flows. *AIAA J.* **60**, 4302–4324.

MODESTI, D. & PIROZZOLI, S. 2016 Reynolds and mach number effects in compressible turbulent channel flow. *Int. J. Heat Fluid Flow* **59**, 33–49.

MODESTI, D., SATHYANARAYANA, S., SALVADORE, F. & BERNARDINI, M. 2022 Direct numerical simulation of supersonic turbulent flows over rough surfaces. *J. Fluid Mech.* **942**, A44.

MUPPIDI, S. & MAHESH, K. 2012 Direct numerical simulations of roughness-induced transition in supersonic boundary layers. *J. Fluid Mech.* **693**, 28–56.

NARDINI, M., JELLY, T. O., KOZUL, M., SANDBERG, R. D., VITT, P. & SLUYTER, G. 2024 Direct numerical simulation of transitional and turbulent flows over multi-scale surface roughness—part ii: The effect of roughness on the performance of a high-pressure turbine blade. *J. Turbomach.* **146** (3).

NICHOLS, J. W., LARSSON, J., BERNARDINI, M. & PIROZZOLI, S. 2017 Stability and modal analysis of shock/boundary layer interactions. *Theor. Comp. Fluid Dyn.* **31** (1), 33–50.

NIKURADSE, J. 1933 Laws of flow in rough pipes. *Tech. Rep.* Technical Memorandum 1292. National Advisory Committee for Aeronautics.

ORLANDI, P. & LEONARDI, S. 2006 Dns of turbulent channel flows with two-and three-dimensional roughness. *J. Turbul.* (7), N73.

PAPAMOSCHOU, D. & ROSHKO, A. 1988 The compressible turbulent shear layer: an experimental study. *J. Fluid Mech.* **197**, 453–477.

PÉREZ-RÀFOLS, F. & ALMQVIST, A. 2019 Generating randomly rough surfaces with given height probability distribution and power spectrum. *Tribol. Int.* **131**, 591–604.

PIROZZOLI, S., BERNARDINI, M. & GRASSO, F. 2008 Characterization of coherent vortical structures in a supersonic turbulent boundary layer. *J. Fluid Mech.* **613**, 205–231.

PRINCE, S. A., VANNAHME, M. & STOLLERY, J. L. 2005 Experiments on the hypersonic turbulent shock-wave/boundary-layer interaction and the effects of surface roughness. *Aeronaut. J.* **109**, 177–184.

RAHIMI, A. & RECHT, B. 2007 Random features for large-scale kernel machines. *Adv. Neural Inf. Process Syst.* **20**.

RASMUSSEN, CARL EDWARD & WILLIAMS, CHRISTOPHER K. I. 2006 *Gaussian Processes for Machine Learning*. Cambridge, MA: MIT Press.

RAUPACH, M. R., ANTONIA, R. A. & RAJAGOPALAN, S. 1991 Rough-wall turbulent boundary layers .

SCHULTZ, M. P. & FLACK, K. A. 2007 The rough-wall turbulent boundary layer from the hydraulically smooth to the fully rough regime. *J. Fluid Mech.* **580**, 381–405.

SPINA, E. F., SMITS, A. J. & ROBINSON, S. K. 1994 The physics of supersonic turbulent boundary layers. *Annu. Rev. Fluid Mech.* **26** (1), 287–319.

TRETEL, A. & LARSSON, J. 2016 Mean velocity scaling for compressible wall turbulence with heat transfer. *Phys. Fluids* **28** (2).

TYSON, C. J. & SANDHAM, N. D. 2013 Numerical simulation of fully-developed compressible flows over wavy surfaces. *Int. J. Heat Fluid Flow* **41**, 2–15.

VAN AMERSFOOR, J., SMITH, L., JESSON, A., KEY, O. & GAL, Y. 2021 On feature collapse and deep kernel learning for single forward pass uncertainty. *arXiv preprint arXiv:2102.11409* .

VOLINO, R. J., FRITSCH, D., DEVENPORT, W. J., EÇA, L., GARCÍA-MAYORAL, R., McKEON, B. J., PIOMELLI, U., CHUNG, D., VISHWANATHAN, V., KERKVLIET, M. & OTHERS 2024 Effects of roughness on non-equilibrium turbulent boundary layers. *J. Turbul.* **25** (10-11), 369–385.

VREMAN, A. W. 2004 An eddy-viscosity subgrid-scale model for turbulent shear flow: Algebraic theory and applications. *Phys. Fluids* **16**, 3670–3681.

WHITEHOUSE, D. J. 2023 *Handbook of surface metrology*. Routledge.

WILLIAMSON, J. B. P., PULLEN, J., HUNT, R. T. & LEONARD, D. 1969 The shape of solid surfaces. *Surface Mechanics, ASME, New York* pp. 24–35.

YANG, X.I.A. & Lv, Y. 2018 A semi-locally scaled eddy viscosity formulation for les wall models and flows at high speeds. *Theor. Comp. Fluid Dyn.* (5), 617–627.

YANG, X.I.A., URZAY, J., BOSE, S. & MOIN, P. 2018 Aerodynamic heating in wall-modeled large-eddy simulation of high-speed flows. *AIAA J.* **56**, 731–742.

YU, C. & LIU, B. 2002 A backpropagation algorithm with adaptive learning rate and momentum coefficient. In *Proceedings of the 2002 International Joint Conference on Neural Networks (IJCNN 2002)*, vol. 2, pp. 1218–1223. Honolulu, HI, USA: IEEE.

YU, M., XU, C. & PIROZZOLI, S. 2019 Genuine compressibility effects in wall-bounded turbulence. *Phys. Rev. Fluids* **4** (12), 123402.

YUAN, J. & PIOMELLI, U. 2014 Roughness effects on the reynolds stress budgets in near-wall turbulence. *J. Fluid Mech.* **760**, R1.

YUAN, Y. & LOZANO-DURÁN, A. 2025 Dimensionless learning based on information. *Nat. Commun.* **16** (1), 9171.

ZHANG, C., DUAN, L. & CHOUDHARI, M. M. 2018 Direct numerical simulation database for supersonic and hypersonic turbulent boundary layers. *AIAA J.* **56** (11), 4297–4311.

ZHANG, Y., BI, W., HUSSAIN, F. & SHE, Z. 2014 A generalized reynolds analogy for compressible wall-bounded turbulent flows. *J. Fluid Mech.* **739**, 392–420.

ZHOU, Z., LI, S., HE, G. & YANG, X. 2024 A data-driven distributed force model for wall-modeled large-eddy simulations of rough-wall turbulence. *J. Comput. Phys.* **514**, 113241.